EUROPEAN FUSION DEVELOPMENT AGREEMENT

EFDA–JET–PR(05)17

W. Fundamenski, R.A.Pitts and JET EFDA contributors

A Parallel Transport Model of Tokamak Power Exhaust Transients

A Parallel Transport Model of Tokamak Power Exhaust Transients

W. Fundamenski[1], R.A.Pitts[2] and JET EFDA contributors*

[1]*EURATOM/UKAEA Fusion Association, Culham Science Centre, Abingdon, OX14 3DB, UK*
[2]*CRPP, Assoc. Euratom-EPFL, CH-1015, Lausanne, Switzerland*
** See annex of J. Pamela et al, "Overview of JET Results",*
(Proc.20 th IAEA Fusion Energy Conference, Vilamoura, Portugal (2004).

Preprint of Paper to be submitted for publication in
Plasma Physics and Controlled Fusion

ABSTRACT

In many tokamak power exhaust transients, eg. Edge Localised Modes (ELMs), thermal quench of disruptions and intermittent SOL bursts (so called blobs), thermal energy is largely removed to divertor or limiter tiles by parallel transport in semi-collisionless plasma filaments. Such transient parallel losses are governed by the coupled Fokker-Planck and Maxwell's equations. While numerical simulations of this system are now becoming available, they are still computationally expensive (CPU time in days) and require specialist support. In this paper, two simplified parallel loss models are developed, one based on the kinetic, the other on the moment or fluid approach. The two models can be combined to form a kinetic-fluid hybrid, whose accuracy can be further improved by using fitting parameters to best match the available kinetic results. This contribution demonstrates that such simple models can capture most of the salient features of kinetic simulations at substantial savings in both cost and complexity (CPU time in seconds). They may be used either as stand alone interpretive tools or as modules in larger turbulence and/or transport codes. As shown here, the fluid model can successfully reproduce ELM filament densities and electron energies measured at the outer poloidal limiter on JET, as well as recent measurements of far-SOL ELM filament ion energies on JET. Taking confidence from this favourable comparison, it is then used to predict the ion impact energies in Type-I ELM filaments on ITER.

1. INTRODUCTION

Transient power loads on plasma facing components due to energetic plasma relaxations, such as Edge Localised Modes (ELMs), Thermal Quench of Disruptions (TQD) and to a lesser extent intermittent turbulent bursts (or blobs), are a cause for concern for next step magnetic confinement fusion reactors; characterising, understanding and eventually mitigating their effects is recognised as one of the most pressing problems in tokamak plasma physics [43, 28, 4]. In both ELMs and TQDs, thermal energy is predominantly removed by parallel transport to plasma facing components, which occurs transiently in semi-collisionless, highly elongated plasma filaments. Since modelling transient parallel losses requires computationally costly kinetic simulations, it is desirable to develop simple models of transient energy evolution, which could be included in existing fluid and turbulence codes. The development of two such models, based respectively on the kinetic and fluid approximations, is the aim of the present study.

The conceptual construct of a filament calls for a short comment: it is neither an ideal flux tube nor a magnetic field line. Instead, a plasma filament may stretch and shear in the perpendicular plane as it propagates radially and may eventually disintegrate into ever smaller filaments, which is especially true in the open field line (SOL) region [12, 33]. Nonetheless, it is useful to consider the evolution of the average thermodynamic quantities of the plasma filament, much as one speaks of eddies or vortices in a turbulent fluid. In section 3, we will describe filament propagation by a simple advective-diffusive model.

2. MOTIVATION: PARALLEL TRANSPORT DURING TOKAMAK TRANSIENTS

2.1 EDGE LOCALISED MODES

Aside from sawteeth, ELMs are the most common plasma transients in many present day tokamaks and form an integral feature of the H-mode confinement regime [43, 81, 8]. ELMs are plasma relaxations thought to originate due to an interaction of two MHD modes: the peeling mode driven by the magnetic shear (or plasma current) and the ballooning mode driven by the pressure gradient [71, 7]. An ELM leads to a rapid drop in density and temperature of the edge (or pedestal) plasma, typically ejecting several percent of the plasma stored energy on some local MHD time scale. Unless otherwise specified, the term ELM will refer to Type-I ELMs, since Type-III ELMs are much smaller and pose a lesser hazard to plasma facing components.

The typical chronology of a Type-I ELM on JET is shown in Fig.2.1; the temporal extent of the plot is 2ms. The start of the MHD activity, measured by a magnetic pick-up coil near the top of the machine, is quickly (<10μs) followed by soft X-ray signals in the main chamber and from the inner divertor CFC tiles, indicating a burst of energetic electrons. The arrival of the bulk plasma pulse in the divertor, measured by divertor D_α and Langmuir probes, is typically delayed due to ion inertia by ~ 100μs and is found to scale with the parallel transit time at the pedestal sound speed, $\tau_{\parallel,ped} \sim L_\parallel / c^{s,ped}$, which we denote as the sonic timescale [56]. The pedestal stored energy decays on the MHD timescale, tMHD ~ 200–300μs, which is typically comparable or larger than the sonic timescale [54, 7]. The ELM size (as measured by the normalised pedestal energy drop $\Delta W_{ELM}/W_{ped}$) is closely (and inversely) correlated to the pedestal collisionality $\nu^*_{i,ped}$ and $\tau_{\parallel,ped}$, which suggests a major role played by parallel losses [54, 55]. For an accessible overview of ELM experimental data the reader is referred to [8].

Let us consider the evolution of the ELM in the framework of the peeling-ballooning model. The MHD ballooning activity associated with the ELM is strongest on the bad curvature, low field side of the plasma, while the MHD peeling modes are strongest in the X-point region. This is consistent with the experimental observation that Type-I ELMs eject (transport) particles and energy into Scrape-Off Layer (SOL) mainly on the outboard side, from where they are carried by parallel and diamagnetic transport to the divertor targets. The strongest evidence for the outboard origin of ELMs is the fact that in double-null equilibria virtually all the ELM power arriving in the divertor is deposited on the outer target [60, 22].

At this point, it is important to distinguish between the ELM as a coherent MHD eigenmode, typically with toroidal mode numbers ~5–20, and the ELM filaments which are the effects of that phenomenon in the SOL [8, 26]. In this picture, the evolution of the ELM may be divided into three stages, which are illustrated schematically in Fig.2.2 and Fig.2.3:

- *MHD stage:* the ELM evolves by developing ~5–20 flute-like ripples in the pedestal thermodynamic and field quantities (the perpendicular perturbations associated with the peeling-ballooning mode). When these disturbances are weak, we speak of linear-MHD, when they are comparable to the ambient quantities, of non-linear MHD. Top frame of Fig.2.2.

- *Transport stage:* As the MHD disturbances grow in magnitude, transport effects become pronounced and lead to saturation of the instability [15]. The initial flute-like perturbations thus evolve into distinct plasma filaments, a situation typical in many interchange and Rayleigh-Taylor instabilities. The observation of such filamentary structures on several large tokamaks [67, 36, 30, 17, 27, 47, 27] is a relatively recent discovery. The filaments experience strong radial forces, propagate outwards with radial velocities ~0.5 – 1km/s and at some point intersect the pre-ELM separatrix, entering the SOL. At this point the initially closed filaments are either opened by a form of peeling or reconnection at the X-point or their energy content is conducted to the existing (pre-ELM) SOL plasma, which might involve the shearing, and gradual disintegration of the filaments [12]. The former theory has been proposed by [72], who notes that the Kadomtsev (or reconnection) time at the X-point is in the range 10 – 100μs for nominal JET ELMs. It applies the ideas developed for sawtooth collapse by field line reconnection in the core plasma to the X-point region [15] and is supported by evidence of strike point movement during particularly large ELMs on JET [73]. The latter theory, often illustrated by drawing an analogy between a rotating filament and a leaky hose, has been as suggested by [82]. The compression of magnetic flux surfaces at the front of the expanding filament is suggested as the mechanism responsible for increased radial transport to the ambient SOL plasma. Middle frame of Fig.2.2.
- *Exhaust stage:* Having crossed the pre-ELM separatrix, the filaments continue to propagate radially and expand in the perpendicular plane, most likely breaking up into ever smaller structures [12]. In addition they experience strong parallel losses to the divertor targets and increasing collisional effects, such as viscosity, conductivity and energy coupling between the ion and electron channels. Bottom frame of Fig.2.2.

We will refer to the above picture of the ELM as the MHD-Transport-Exhaust (MTE) model. The evolution of the outer mid-plane radial density (pressure) profiles are illustrated schematically in Fig.2.3, where the pre-ELM and post-ELM profiles are also indicated. Note that the peak filament quantities are reduced both by expansion and by parallel losses. The transfer of energy from the closed (core) to the open (SOL) filaments is often obscured or glossed over in the topical literature. Yet, this mechanism is essential to explain the observation that most of the ELM energy arrives at the divertor targets, rather than being deposited on the vessel wall [25, 55]. It thus appears that during the ELM crash the thermal energy of the pedestal plasma is conveyed to the divertor targets by parallel convection and conduction within the ELM filaments and to the main chamber limiters by radial propagation of the filaments themselves. Therefore, from the practical point of view (heat loads on divertor and limiter tiles) the open ELM filaments are equally important as the original flute-like perturbation. The specific aim of this article is to develop a model which follows the individual open ELM filaments as they propagate in the SOL in order to estimate the decay of their density and energy due to parallel losses.

In order to justify the MHD-Transport-Exhaust (MTE) model of an ELM, it is necessary to show that typical MHD timescale of the ELM and the average sonic timescale of the filaments, $\langle\tau_{\|}\rangle$ are comparable, such that both MHD and Exhaust processes determine the evolution of the ELM. Here we should not confuse the duration of MHD activity, measured by τ_{MHD}, with the filament formation time which is presumably much smaller. If tMHD was much larger than $\langle\tau_{\|}\rangle$, many generations of filaments would have to be formed, each one being drained by parallel losses as quickly as it is formed. The Exhaust phase would thus be largely irrelevant and all the energy ejected into the SOL would appear directly on the divertor tiles. Conversely, if τ_{MHD} was much smaller than $\langle\tau_{\|}\rangle$, only one generation of filaments would be (instantaneously) born, whose particle and energy content would then be gradually depleted by parallel losses. Since $\tau_{MHD} \sim \langle\tau_{\|}\rangle \sim 200-300\mu s$ for typical Type-I ELMs on JET, we expect that both MHD and Exhaust physics play a role in ELM evolution. On the strength of this observation, we expect that only by including both effects can we hope to quantify the size of the ELM and the partition of its energy between the divertor and limiter targets.

To this end, we examine the scaling of the two timescales with plasma dimensionless variables. The MHD timescale of the ELM may be estimated as the transport-limited MHD growth time [7],

$$\tau_{MHD} \sim (\tau_{A,ped}^{\ 2}\,\tau_{E,ped})^{1/3} \tag{2.1}$$

where $\tau_{A,ped}$ is the pedestal Alfven time,

$$\tau_{A,ped} \sim L_{\|}/v_{A,ped} \sim \pi R q_{95}/v_{A,ped} \tag{2.2}$$

and $v_{A,ped}$ is the pedestal Alfven speed. The parallel connection length $L_{\|} \sim \pi R q_{95}$ is estimated using the major radius R and the safety factor at the 95% poloidal flux surface, q_{95}. Note that the Alfven time is shorter than a typical sonic time, $\tau_{\|,ped} \sim L_{\|}/c_{s,ped} \sim \pi R q_{95}/c_{s,ped}$, where $c_{s,ped}$ is the pedestal plasma sound speed, their ratio being equal to the square root of the plasma beta,

$$\tau_{A,ped}/\tau_{\|,ped} \sim c_{s,ped}/v_{A,ped} \sim \beta_{ped}^{\ 1/2} \tag{2.3}$$

and $\beta_{ped} \sim 0.01$ in large aspect ratio tokamaks (hence $\beta_{ped}^{\ 1/2} \sim 0.1$).
The upper limit on τ_{MHD} may be obtained by setting $\tau_{E,ped} = \langle\tau_E\rangle$, where $\langle\tau_E\rangle$ is the global energy confinement time,

$$\langle\tau_E\rangle = \int W dV/P_{SOL}, \qquad W \equiv 3/2 \times n(T_e + T_i) \tag{2.4}$$

where $\int dV$ denotes an integral over the core plasma volume and P_{SOL} is the power crossing the separatrix, i.e. entering the Scrape-Off Layer (SOL). The lower limit on τ_{MHD} is found with $\tau_{E,ped} = \tau_{E,nc}$, where $\tau_{E,nc}$ is the pedestal neo-classical energy transport time,

$$\tau_{E,nc} \sim W_{ped}/(\partial W_{ped}/\partial t) \sim W_{ped}/(\nabla_\perp n\chi_{nc}\nabla_\perp T_i) \sim 3/2\times\Delta_{ped}{}^2/\chi_{nc} \quad (2.5)$$

Here Δ_{ped} is the pedestal width and cnc is the pedestal neo-classical (ion) heat diffusivity. We evaluate cnc at the transition between the banana and Pfirsch-Schlueter regimes (the plateau regime being absent when the inverse aspect ratio $\varepsilon = a/R$ is greater than ~ 0.2 [39]),

$$\chi_{nc} \approx 1.5\varepsilon^{1/2}\rho_{\theta i}{}^2/\tau_{ii} \approx q_{95}{}^2\rho_i{}^2/\tau_{ii} \quad (2.6)$$

where ρ_i and $\rho_{\theta i}$ are the total and poloidal ion gyro-radii and tii is the ion-ion collision time. Using this expression, we obtain the following estimate for the MHD time,

$$\tau_{MHD}{}^{min}/\tau_{A,ped} \sim \beta_{ped}{}^{-1/6}(\tau_{E,ped}/\tau_{\|,ped})^{1/3} \quad (2.7)$$

Substituting (2.3) and (2.5), this ratio can be expressed in dimensionless form as,

$$\tau_{MHD}{}^{min}/\tau_{A,ped} \sim \varepsilon^{-1/6}\beta_{ped}{}^{-1/6}\nu^*{}_{i,ped}{}^{-1/3}\rho^*{}_{\theta i,ped}{}^{-2/3} \quad (2.8)$$

or

$$\tau_{MHD}{}^{min}/\tau_{A,ped} \sim 1.15\times q_{95}{}^{-2/3}\beta_{ped}{}^{-1/6}\nu^*{}_{i,ped}{}^{-1/3}\rho^*{}_{i,ped}{}^{-2/3} \quad (2.9)$$

where the ion pedestal collisionality $\nu^*{}_{i,ped}$ and the pedestal width-normalised ion gyro-radii, $\rho^*{}_{\theta i,ped}$ and $\rho^*{}_{i,ped}$, are defined as

$$\nu^*{}_{i,ped} = L_\|/\lambda_{ii,ped} \sim L_\|/\chi_{s,ped}\tau_{ii,ped}, \qquad \rho^*{}_{\theta i,ped} = \rho_{\theta i}/\Delta_{ped}, \qquad \rho^*{}_{i,ped} = \rho_i/\Delta_{ped} \quad (2.10)$$

In Table 2.1, the above expressions are evaluated for nominal JET and ITER values. It is worth noting the emerging hierarchy of time scales,

$$\tau_{A,ped} << \tau_{\|,ped} << \tau_{ii,ped} << \tau_{E,nc} << \langle\tau_E\rangle \quad (2.11)$$

ranging from micro-seconds for tA,ped to seconds for $\langle\tau_E\rangle$. In both tokamaks, the top of the pedestal is collisionless, $\nu_{i,ped}{}^* \sim L_\|/\lambda_{ii,ped} \sim 0.02-0.04$, while the separatrix is semi-collisional, $\nu_{i,sep}{}^* \sim L_\|/\lambda_{ii,sep} \sim 1$. Therefore, we expect kinetic effects to play an important role in ELM dynamics in both JET and ITER.

The upper limit on τ_{MHD} is obtained from (2.1) and (2.4), assuming $\langle\tau_E\rangle_{JET} \sim 0.4$s and $\langle\tau_E\rangle_{ITER} \sim 3.8$s, which yields $\tau_{MHD}{}^{max} \sim 240\mu$s for JET and $\tau_{MHD}{}^{max} \sim 690\mu$s for ITER. The lower limit, that is (2.1) with (2.5), depends on the value of the pedestal width. Assuming a nominal value of 25mm for

JET yields τ_{MHD}^{min} ~100μs. For ITER, τ_{MHD}^{min} is evaluated for two simple (and often cited) scalings of the pedestal width, $\Delta_{ped}/R = 0.025$ and $\Delta_{ped}/\rho_{\theta i,ped} = 2.5$, which predict $\Delta^{ped} = 50$ and 21mm, respectively; the former of these is the reference ITER prediction, while the latter is the purely neo-classical or ion orbit loss scaling. The corresponding MHD times are found as τ_{MHD}^{min} ~300μs and τ_{MHD}^{min} ~170μs. The results are summarised in Table 2.2. The observed MHD ELM times on JET, which are typically measured as τ_{MHD} ~200–300μs [54, 7] are in good agreement with the upper limit estimate, τ_{MHD}^{max} ~240μs and a factor of 2–3 larger then the lower limit estimate, τ_{MHD}^{min} ~ 100μs. These times should be compared with the average sonic times for the filaments, which we estimate as $\langle\tau_{||}\rangle \sim (\tau_{||0}\tau_{||lim})^{1/2}$, where $\tau_{||0}$ is the initial parallel loss time, evaluated at the pedestal, and tlllim, the final parallel loss time, evaluated just before the filaments intersect the limiter. Assuming T_{lim} ~50eV on JET and ~100eV on ITER, we find $\langle\tau_{||}\rangle_{JET} \sim 190$μs and $\langle\tau_{||}\rangle_{ITER}$ ~320μs. We thus find that

JET:	$\tau_{MHD}^{min}/\langle\tau_{||}\rangle \sim 0.4,$	$\tau_{MHD}^{max}/\langle\tau_{||}\rangle \sim 1$
ITER:	$\tau_{MHD}^{min}/\langle\tau_{||}\rangle \sim 0.5 - 0.95,$	$\tau_{MHD}^{max}/\langle\tau_{||}\rangle \sim 2$

such that MHD and exhaust physics evolve on comparable timescales. We may speculate that τ_{MHD}^{min} corresponds to filament formation time, while tMHDmax to the duration of all MHD activity, which would indicated that filaments are indeed formed faster than they can be diluted by parallel losses. Since the assumption of rapidly born filaments is central to the development of the parallel loss model of the ELM, one of the main aims of the present article, it is encouraging to find that this assumption to be consistent with known plasma physics.

As a final remark on ELM, we note that the above analysis largely justifies the proposed MTE picture of the ELM. In practice, one is still forced to separate the physics into the MHD and Exhaust parts, as is in fact done in this article where the MHD stage is not explicitly addressed. However, this should not detract us from realising that an integrated model of the ELM is ultimately necessary for fully consistent predictions.

2.2 THERMAL QUENCH IN DISRUPTIONS

A tokamak discharge may terminate with a rapid loss of magnetic equilibrium and stored energy in a so called plasma disruption. A short but clear introduction to tokamak disruptions may be found in [82]; for more detailed reviews see [68, 65]. There are several types of disruptions, and several stages in the disruption itself, reflecting the complexity of this most violent of tokamak transients. One of these stages, the so-called thermal quench phase of a disruption (TQD) during which most of the plasma stored energy is lost, generally precedes the current quench phase and occurs on much faster, typically MHD (Alfvenic-sonic) timescales, see Section 2.1. This time scale is too short to be explained by radiation alone, and it has been suggested that energy is largely removed by parallel transport [82]. This is supported by the observation of a radially accelerating helical perturbation acting as a precursor

to a TQD in high beta plasmas with internal transport barriers [63]. The TQD onset begins when this core filament protrudes beyond the separatrix and comes into contact with outboard limiters. Such an explosive instability has been theoretically predicted in the non-linear evolution phase of the MHD ballooning mode [23]. Infra-red thermography and divertor thermocouples show that the energy removed during TQD is deposited on both the divertor and limiter tiles [59, 64]; observation of after-glow heat on main chamber walls of the MAST tokamak suggests this deposition is spatially localised and occurs via a helical filament excursion [47]. Since the intense heat loads associated with the TQD could lead to ablation and melting of plasma facing components, mitigating their effects has been identified as a high priority task for future reactors, including ITER [29].

The typical chronology of a TQD on JET is shown in Fig.2.4; the temporal extent of the plot is 10 ms, with a minor TQD occurring at 27.194s, followed by a major TQD at ~ 27.197s. The plasma current remains unchanged during both events, suggesting the TQD occurs too quickly to change the magnetic equilibrium of the discharge. The MHD activity is much more pronounced during the second TQD phase in Fig.2.4. The start of this activity is coincident with a burst of energetic electrons at the inner target (soft X-ray signal). This is quickly followed by the drop of the plasma stored energy, which decays exponentially with a time constant of ~ 200 ms, comparable to the parallel sonic transit time, $\tau_{\|} \sim 100\mu s$. The Da light at the outer mid-plane and in the outer divertor, associated with the bulk plasma pulse and related recycling at the solid targets, is delayed by $500-1000\mu s$ with respect to the electron burst. The overall behaviour is similar to that of a Type-I ELM discussed in the previous section. It should be emphasised that temporal-spatial evolution of the TQD pulse remains largely undiagnosed, and may involve stochastic mixing (radial ergodisation) of magnetic field initially forming a flux surface.

2.3 SOL INTERMITTENCY

At the other end of the energy spectrum, tokamak plasmas are constantly subjected to micro-transients associated with turbulence. While the TQD ejects nearly all the plasma stored energy, $\Delta W_{TQD}/W \sim 1$, an ELM typically several percent, $\Delta W_{ELM}/W \sim 10^{-2}$, the intermittent turbulent bursts observed in the SOL are typically much smaller, $\Delta W_{SOL}/W \sim 10^{-6} - 10^{-4}$. Since the frequency of these transients scales roughly inversely with their size, $f_{TQD} \sim 0.1$Hz, $f_{ELM} \sim 10$Hz and $f_{SOL} \sim 10^3 - 10^5$Hz, the resulting time-averaged powers, $P \sim f_{DW}$, are comparable for the three types of transients,

$$\begin{aligned} P_{TQD}/W &\sim f_{TQD}\Delta W_{TQD}/W \sim 0.1\ s^{-1} \\ P_{ELM}/W &\sim f_{ELM}\Delta W_{ELM}/W \sim 0.3\ s^{-1} \\ P_{SOL}/W &\sim f_{SOL}\Delta W_{SOL}/W \sim 0.1\ s^{-1} \end{aligned} \qquad (2.12)$$

The existence of substantial fluctuations of density and temperature in the SOL is well established [44, 42, 75]. Relative size of the fluctuations is larger in the SOL than in the core plasma and larger

still in the far-SOL. The same is true for the level of intermittency, which measures the departure of the probability distribution function away from the normal Gaussian shape [37]. This increasing level of intermittency may be interpreted in terms of plasma filaments (or blobs) propagating radially with velocities of order 1km/s or $v_\perp/c_s \sim 10^{-2} - 10^{-3}$, similar to those measured for ELMs. Such filaments have now been observed on most tokamaks using both Langmuir probes and gas puff imaging. Due to their low energy content, they do not individually pose any danger to the plasma facing components, but their collective action could lead to enhanced material erosion and impurity generation. This is especially true if the ion temperatures in the filaments exceed the threshold for physical sputtering.
The theoretical framework of SOL turbulence appears to well established and capable of explaining the observed phenomenology: two dimensional dynamics of elongated plasma filaments (acting as turbulent eddies) in the plane perpendicular to the magnetic field, increasing intermittency in the far-SOL, turbulence self-regulation via poloidal zonal flow formation, and strong dissipation of energy by parallel losses. Most of these characteristics have been observed in the experiments [77, 2, 41, 17, 28] and have been largely reproduced in numerical simulations of SOL turbulence with different levels of sophistication [10, 83, 69, 51, 24, 34, 34]. However, most SOL turbulence codes rely on the fluid (typically single fluid) approximation, in which the parallel transport of energy to the divertor targets is treated in the most rudimentary fashion.

3. ADVECTIVE-DIFFUSIVE MODEL OF TOKAMAK PLASMA FILAMENTS

In the fluid picture, the spatial-temporal evolution of plasma density and energy is described by dynamical moment equations in advective-diffusive form [18, 40],

$$\begin{aligned}
&\frac{\partial n_a}{\partial t} + \nabla . A_a = S_{n,a}, && A_a = n_a u_a - D_a \nabla n_a \\
&\frac{\partial \varepsilon_a}{\partial t} + \nabla . q_a = S_{\varepsilon,a} + Q_a, && q_a = \left(\tfrac{1}{2} m_a u_a + \tfrac{5}{2} T_a\right) A_a - n_a \div_a \nabla T_a \\
&Q_e = \frac{\varepsilon_i - \varepsilon_e}{\tau_{ie}} - Q_i && \varepsilon_a = \left(\tfrac{1}{2} m_a u_a^2 + \tfrac{3}{2} T_a\right) n_a
\end{aligned} \tag{3.1}$$

where na and ea are the particle and energy densities for species a = i,e, $\mathbf{u}_a$ are flow velocities, $\mathbf{\Gamma}_a$ and $\mathbf{q}_a$ the particle and energy fluxes, D_a and χ_a the particle and heat diffusivities, $S_{n,a}$ and $S_{\varepsilon,a}$ the particle and energy sources and Q_a the energy equipartition term. Note that we have neglected the momentum conservation equation from (3.1); instead, we impose the Mach boundary condition ($M \geq 1$) at the entrance into the sheath and represent parallel losses by effective removal times, see below. Quasi-neutrality requires that $n_e = Zn_i$, $\mathbf{\Gamma}e = Z\mathbf{\Gamma}_i$, $S_{n,e} = Z_{Sn,i}$ where Z is the ion charge. Although this condition can be violated transiently, as will be shown in Section 4, in the context of the fluid approach one may assume it to be satisfied at all times. For a fully ionised hydrogenic plasma, quasi-neutrality requires $n_e = n_i = n$ and $\mathbf{\Gamma}e = \mathbf{\Gamma}_i = \mathbf{\Gamma}$. The fluxes $\mathbf{\Gamma}$ and $\mathbf{q}_a$ involve three orthogonal directions: parallel $\|$, diamagnetic $\wedge$ and radial $\perp$, with the $\|$ and $\wedge$ directions defining the flux surface; provided the system is axis-symmetric ($\partial/\partial\phi \sim 0$), they may be combined into a single, poloidal direction q. However,

it should be noted that plasma transport always occurs in three ($\|$, $\wedge$, $\perp$) rather than two (θ, r) directions, where r is the radial coordinate. The geometry of SOL transport, including the role of classical drifts, is discussed in [19, 75, 31].

In order to study the temporal evolution of (3.1), we can employ the Green's function approach, a comprehensive account of which may be found in [58]. The Green's function, G(r,t) is the response of the dynamical equations to a Dirac delta function impulse, $\delta(r)\delta(t)$. It can be used to construct the response to an arbitrary source, S(r,t) as a spatial and temporal convolution, $S*G = \iint S(r,t)G(r-r',t-t')dr'dt'$. For example, the Green's function for the density response in (3.1) is easily found if $u_\perp$ and $D_\perp$ are assumed constant, and if parallel and diamagnetic divergences are replaced by n/τ_n, denoting poloidal (parallel plus diamagnetic) particle loss with a characteristic decay time τ_n,

$$\left(\frac{\partial}{\partial t} + \frac{1}{\tau_n} + u_\perp \nabla_\perp - D_\perp \nabla_\perp^2 \right) G_n = \frac{d}{dt} G_n = \delta(r)\,\delta(t) \tag{3.2}$$

The solution to (3.2) is easily found as an advected, Gaussian wave-packet [58],

$$G_n(r,t;\tau_n,u_\perp,D_\perp) = \frac{1}{\sqrt{\pi D_\perp t}} \exp\left(- \frac{(r - u_\perp t)^2}{D_\perp t} - \frac{t}{\tau_n} \right)$$

$$n(r,t) = \int_{-\infty}^{t} dt' \int_{0}^{r} dr' G_n (r - r', t - t') \, S(r', t') \tag{3.3}$$

If the diamagnetic divergence term is included explicitly, rather than implicitly via τ_n, $u_\wedge$ and $D_\wedge$ appear in (3.3) in exact symmetry to $u_\perp$ and $D_\perp$,

$$G_n(a,r,t;\tau_{||},u_\perp,D_\perp,u_\square) = \frac{1}{\pi t \sqrt{\pi D_\perp t}} \exp \left(- \frac{(r - u_\perp t)^2}{D_\perp t} - \frac{(\alpha - u_\square t)^2}{D_\square t} - \frac{t}{\tau_{||n}} \right) \tag{3.4}$$

where a is the diamagnetic co-ordinate and t||n is the parallel particle loss time. The above expression defines an elongated plasma filament, whose centre moves in the $\perp - \wedge$ plane with velocities u^ and u$\dot{Y}$, and broadens as $(D_\perp t)^{1/2}$ and $(D_\wedge t)^{1/2}$ in the two directions. This corresponds to the filamentary structures observed in tokamaks during ELMs [26, 48], TQDs [63] and SOL intermittency [78, 17] and shown schematically in Fig.2.2. The temporal evolution of (3.3) is shown graphically in Fig.3.1 for the case of comparable advective and diffusive terms ($u_\perp = D_\perp = 1$) and negligible poloidal losses, $\tau_n >> 1$; it corresponds to the perturbed part of the profiles as illustrated in Fig.2.3. Its maximum decays exponentially with time, and hence also with radius,

$$G_n^{max}\left(t = \frac{r}{u_\perp} \right) = \frac{1}{\pi t \sqrt{\pi D_\perp t}} \exp\left(- \frac{t}{\tau_n} \right) \tag{3.5}$$

while its integral, which represents the total number of particles in the filament, is reduced only by poloidal losses,

$$\int_{-\infty}^{\infty} G_n(t,r)dr = \exp\left(-\frac{t}{\tau_n}\right) = \exp\left(-\frac{r}{\lambda_{n,u}}\right),\ \lambda_{n,u} = u_\perp \tau_n \tag{3.6}$$

The Green's function for the energy response can be similarly derived, although the presence of an additional diffusion term complicates the final expression. The result is a product of convective and conductive parts, where the former is formally identical to (3.4), while the latter follows from (3.4) with the following transformation: $D_{\perp a} \rightarrow \chi_{\perp a}$, $D_{\wedge a} \rightarrow \chi_{\wedge a}$, $\tau_{\|n} \rightarrow \tau_{\|a}$. The energy of the plasma filament is therefore reduced by both convective and conductive transport in all three directions. Specifically, the temperature profile of species a broadens roughly as $(\chi_{\wedge_a} t)^{1/2}$ and $(\chi_{\wedge_a} t)^{1/2}$, which may occur much faster than the broadening of the density profile if $\chi_{\wedge_a} >> D_{\wedge_a}$ (as is the case for classical ion conduction/diffusion).

The dynamics of plasma filaments in the $\perp-\wedge$ plane has been investigated in the context of SOL plasma turbulence and radial ELM propagation [10, 24, 59, 32, 17]. On JET, it was found that ELM filaments propagate radially in the SOL with average velocities between 500 and 1000 m/s. However, the details of radial filament dynamics are not important for the purpose of the present study, in which we adopt the frame of reference moving with the plasma filament in the $\perp-\wedge$ plane. We need only note that in this frame the reduction of integrated particle and energy densities occurs only due to parallel losses (these differ from poloidal losses in the presence of strong radial electric fields, when diamagnetic fluxes become significant) and that peak filament values are additionally reduced by filament expansion in the $\perp-\wedge$ plane, $n_{max}/n \propto (D_\wedge t)^{-1/2}$. In the remainder of the paper, we will adopt this (filament) frame of reference and assume $v_\perp$ and $D_\perp$ are known. For the sake of simplicity, we will treat filament broadening in two stages, initially solving (3.1) with the assumption of $D_\perp = 0$, and introducing filament broadening in the following stage by assuming polytropic expansion. It should be stressed that filaments will be assumed to propagate into vacuum, i.e. the background SOL plasma is ignored. In section 4, we will include this background explicitly to determine the relative change from pre-ELM to ELM fluxes.

4. KINETIC DESCRIPTION OF PARALLEL LOSSES

The problem of transient parallel losses from the plasma to solid surfaces is intimately linked with that of electrostatic (Langmuir) and magnetic (Chodura) sheath formation [22]. In this problem, the velocity distribution functions for ions and electrons, $f_i(\mathbf{v})$ and $f_e(\mathbf{v})$, evolve according to Fokker-Planck and Poisson equations [49, 57, 40]

$$\left(\frac{\partial}{\partial t} + v_{\|a}\nabla_\| + \frac{e_a(E + v_a \times B)}{m_a}\cdot\nabla_v\right) f_a(s,v_a,t) = \sum_{b\in\{i,e\}} C_{ab} + s_a$$
$$\nabla_\|\varphi = -\nabla_\| E_\| = -4\pi(e_e \int f_e dv_e + e_i \int f_i dv_i) \tag{4.1}$$

Here s is the parallel distance,j the electrostatic potential and **v**a, ea and ma the velocity, charge and mass of species a, respectively; **C**ab and **S**a denote inter-species collisions and volumetric sources.

Equations (4.1) are closed by assuming perfect absorption at the plasma-solid interface (s = L||),

$$f_i\,(s = L_{||},\, v_{||i} > 0, t) = f_e\,(s = L_{||},\, v_{||e}\,\nabla_{||} > 0, t) = 0 \qquad (4.2)$$

The sheath problem, being one of the oldest in plasma physics, has been intensively studied, both analytically and numerically [21, 75, 52]. Unfortunately, it is typically solved under steady state conditions, with the additional assumption of zero current flow into the sheath,

$$e_i \text{”} \int f_i v_{||i}\, dv_i = e_e \text{”} \int f_e v_{||e} dv_e = 0$$

Consequently, the existing literature is of limited use for studying the process of sheath formation and the associated transient particle and energy fluxes. To address this issue, a simple model based on the Maxwellian approximation is developed below and compared with recent kinetic simulations in Section 4.2.

4.1 MAXWELLIAN APPROXIMATION

Neglecting collisional effects from (4.1), yields the Vlasov-Poisson problem. This approximation is reasonable for the initial phase of high energy transients such as ELMs and disruptions, eg. for typical JET conditions of $T_{e,ped} \sim 1$keV and $n_{e,ped} \sim 10^{20}$ m^{-3}, the thermal Mean-Free-Path (MFP) exceeds the connection length, $L_{||} \sim 30$m. However, even under moderately collisional conditions, supra-thermal particles may be effectively collisionless due to the strong increase of the Coulomb collisional mfp with particle velocity, $\lambda_{aa}(v) \propto v^4$ [57, 45]. For the same reason, sub-thermal particles are nearly always collisional. Consequently, the approach developed below is only applicable for thermal or supra-thermal velocities.

To further simplify the analysis (and separate the electrostatic and inertial effects in the kinetic equation), we neglect the Coulomb force (set $E_{||} = 0$) on the left hand side of (4.1), effectively decoupling the ion and electron distributions. This leaves a purely magnetic Lorentz force which, in turn, vanishes for parallel motion. As a result, (4.1) reduces to a force-free Vlasov equation. In this approximation, ions and electrons are distinguished only by their masses, their charge having no effect on the parallel dynamics. The resulting problem is formally identical to transient kinetic effusion of gas molecules into a vacuum, which occurs following an explosion or a removal of a separating membrane between two chambers, and has been treated extensively in the kinetic theory of gases [20, 53]. An accessible, modern account of this problem may be found in [35]. Below we briefly show that gas kinetic results provide important insights and a useful starting point for plasma kinetic analysis.

Consider a plasma filament in a tokamak SOL, bounded on either side by perfectly absorbing divertor targets. We define the outer mid plane location as s = 0 and denote the connection lengths to the inner and outer divertor targets as $L_{||i}$ and $L_{||o}$, respectively. The divertor targets are thus located at $s = -L_{||i}$ and $s = L_{||o}$. We would like to determine the temporal evolution of the filament-averaged

density and temperature, as well as the particle and energy fluxes deposited at both divertor targets. This can be obtained by calculating the Green's function of the bounded filament, i.e. the response of the bounded, force-free, Vlasov equation to a delta function impulse, $\mathbf{S}a = \delta(s)\delta(t)f_{M,a}(\mathbf{v})$ where $f_{M,a}(\mathbf{v})$ is a Maxwellian distribution,

(4.3)

Here $v_{T,a}{}^2 = 2_{Ta,0}/m_a$ is the initial thermal speed of species a, and $f_{M,a}(\mathbf{v})$ is normalised to the same value n_0 for both ions and electrons to assure charge equality. This distribution is assumed stagnant, $u_i = u_e = 0$ ($u_a \equiv u_{a||}$ is the parallel velocity), and isotropic, $T_{||a,0} = T_{\perp a,0} = T_{a,0}$, with potentially different ion and electron temperatures, $T_{i,0}$ and $T_{e,0}$. In (4.3) and the rest of the section, the subscript 0 refers to the initial (t = 0) value of any quantity and $\perp$ denotes both directions perpendicular to B. Consequently, $\mathbf{v}_\perp$ is a vector in the $\perp-\wedge$ plane and $T_{\perp a,0}$ is the temperature associated with the particle gyration.

In the force-free, Vlasov equation,

$$\frac{\partial n_a}{\partial t} + v_{||}\nabla_{||}\ f_a = \frac{d}{dt}\ f_a = S_a \tag{4.4}$$

the left hand side forms an advective time derivative, so that $f_a(t,s,v_{||},v_\perp)$ evolves due to free streaming of particles with constant velocities $v_{||}$. This leads to a net dispersion of the initial Maxwellian distribution, with each element $f_{M,a}(v_{||},v_\perp)d\mathbf{v}$ being translated to $s = v_{||}t$ after time t. By this time, all particles with $v_{||} > L_{||o}/t$ have been lost to the outer target and those with $v_{||} < -|L_{||i}/t|$ have been lost to the inner target. As a result, the distribution is progressively depleted at both ends, with the fastest, most energetic particles being lost first. In the absence of forces and collisions, a particle initially travelling towards the outer target will eventually terminate there. The loss of particles to the two targets can therefore be treated separately by defining the critical velocity $v_{cr}(t) = L_{||}/t$, where $L_{||}$ may denote the connection length to either target. The fraction of particles remaining in the filament after time t, $(n/n_0)a$ which constitutes the desired Green's function for density evolution G_n, is found by integrating $f_{M,a}(\mathbf{v})$ from 0 to $v_{cr}(t)$ and dividing by the initial value,

$$G_n(x_a) = \left(\frac{n}{n_0}\right) = \frac{\int_{0}^{-\infty v_{cr}} f_{M,a}(v_{||}, v_\perp)dv_{||}dv_\perp}{\int_{-\infty}^{-\infty 0} f_{M,a}(v_{||}, v_\perp)dv_{||}dv_\perp} = \mathrm{erf}\,(x_a),\ \ x_a = \beta_a^{\frac{1}{2}}v_{cr} = \frac{v_{cr}}{v_{T,a}} = \frac{L_{||}}{v_{T,a}} = \frac{\tau_{||a}}{t} \tag{4.5}$$

where erf(x) is the error function, $\tau_{||a} = L_{||}/v_{T,a}$ the thermal transit time, and x_a the critical velocity normalised by $v_{T,a}$ and/or the inverse time in units of t||a. It is noteworthy that G_n depends on t, $L_{||}$,

$T_{a,0}$ and ma via a single combination of these variables, namely x_a. This implies, for instance, that a spatially distributed source, $S_n(L_{||})$ is formally equivalent to a temporal source $S_n(t)$ with equivalent transit times. This fact can be used to reduce the convolution S*G to a single integral over xa.

Similarly, the fraction of energy remaining in the filament after time t, $(\varepsilon/\varepsilon_0)_a$ and hence the Green's function for energy evolution are found as

$$G_\varepsilon(x_a) = \left(\frac{\varepsilon_0}{\varepsilon_0}\right) = \left(\frac{\varepsilon_{||} + \varepsilon_\perp}{\varepsilon_0}\right) = \frac{\int_{-\infty}^{0}\int f_{M,a}(v_{||}, v_\perp)dv_{||}dv_\perp}{\int_{-\infty}^{0}\int f_{M,a}(v_{||}, v_\perp)dv_{||}dv_\perp} = \mathrm{erf}(x_a) - \frac{2}{3\sqrt{\pi}}\, x_a e^{-x_a^2} \qquad (4.6)$$

In the above integral, the energy associated with gyration $\varepsilon_\perp$ is only reduced due to particle losses, whereas parallel energy $\varepsilon_{||}$ is reduced more quickly due to preferential loss of supra-thermal particles. If we define the corresponding temperatures as $3T_{\perp a}/2 = \varepsilon_{\perp a}/n$ and $3T_{||a}/2 = \varepsilon_{||a}/n$, we find that $T_{\perp a}$ remains constant at $T_{a,0}$, while $T_{||a}$ is reduced due supra-thermal losses,

$$\left(\frac{T_\perp}{T_0}\right)_a = 1, \quad \left(\frac{T_{||}}{T_0}\right)_a = \frac{(\varepsilon_{||}/\varepsilon_{||0})_a}{(n/n_0)_a} = 1 - \frac{2}{\sqrt{\pi}} \cdot \frac{e_a e^{-x_a^2}}{\mathrm{erf}(x_a)} \qquad (4.7)$$

The effective temperature is an average of$T_{\perp a}$ and $T_{||a}$, with the former being counted twice due to two degrees of freedom associated with the gyrating motion,

$$\left(\frac{T}{T_0}\right)_a = \left(\frac{2T_\perp T_{||}}{3T_0}\right)_a = \frac{2}{3} + \frac{1}{3}\left(\frac{T}{T_0}\right)_a = 1\,\frac{2}{3\sqrt{\pi}} \cdot \frac{x_a e^{-x_a^2}}{\mathrm{erf}(x_a)}\,\frac{(\varepsilon/\varepsilon_0)_a}{(n/n_0)_a} \qquad (4.8)$$

The above results are plotted in Fig.4.1 vs. $t/\tau_{||a} = x_a^{-1}$. The decay of all quantities is delayed with respect to a pure exponential, $\exp(-t/\tau_{||a})$, the solution to $dn/dt = -n/\tau_{||a}$, which is also shown in Fig.4.1; we will exploit this delay in the fluid approximation, Section 5. All functions approach unity for $xa >> 1$ ($t << \tau_{||a}$) and zero for $x_a << 1$ ($t >> \tau_{||a}$), with the exception of T_a which has an asymptotic limit of 2/3. Energy and parallel temperature are reduced much faster than density, but only $T_{||a}$ approaches pure exponential decay. Parallel temperature decays to half its initial value in one thermal transit time, $(T_{||}/T_0)a = 0.5$ at $x_a \sim 1$, energy takes $\sqrt{2}$ times longer, $(\varepsilon/\varepsilon_0)a = 0.5$ at $x_a \sim 1/\sqrt{2}$, and density twice as long, $(n/n_0)_a = 0.5$ at $x_a \sim 0.5$.

Under steady-state conditions, the (uni-directional) particle and energy fluxes for a half-Maxwellian distribution, which we denote as Ga• and qa• respectively, can be integrated to yield

$$\begin{aligned}
\Gamma_a^\infty &= \int_{-\infty}^{\infty}\int_{0}^{\infty} v_{||} f_{M,a}(v_{||}, v_\perp)dv_{||}dv_\perp = \frac{1}{4}\cdot\frac{2}{\sqrt{\pi}}\cdot n v_{T,a} \\
q_{||a}^\infty &= \int_{0}^{\infty}\int_{-\infty}^{\infty} \tfrac{1}{2} m_a v_{||}^2 v_{||} f_{M,a}(v_{||}, v_\perp)dv_{||}dv_\perp = T_a \Gamma_a^\infty = q_{\perp a}^\infty \\
q_a^\infty &= q_{||a}^\infty + q_{\perp a}^\infty = \int_{-\infty}^{\infty}\int_{0}^{\infty} \tfrac{1}{2} m_a (v_{||}^2 + v_\perp^2)\, v_{||} f_{M,a}(v_{||}, v_\perp)dv_{||}dv_\perp = 2T_a \Gamma_a^\infty \\
\therefore \gamma_a^\infty &\equiv \frac{q_a^\infty}{T_a \Gamma_a} = 2, \qquad M_{||}^\infty \equiv \frac{\Gamma_a}{n v_{Ta}} = \frac{1}{4}\frac{2}{\sqrt{\pi}} = 0.28
\end{aligned} \qquad (4.9)$$

The effusion velocity is subsonic, $M_{||}^{\infty} < 1$, and on average, the free streaming particles remove $2T_a$ of kinetic energy from the plasma, with equal contributions from perpendicular and parallel energies.

Under transient conditions, the particle and energy fluxes striking the divertor target, and hence the corresponding Green's functions, may be obtained in two different ways. The first, more direct method is to note that in the time interval between t and dt only those particles with $v_{cr} < v_{||} < v_{cr} + dv_{cr}$ reach the divertor target. Since the number of particles in that interval is $f_{M,a}(v_{cr})dv_{cr}$, the rate of particle loss is equal to $f_{M,a}(v_{cr})dv_{cr}/dt$. Substituting for $f_{M,a}(v)$ and evaluating $dv_{cr}/dt = d/dt(L_{||}/t) = -v_{cr}/t$, we find $\Gamma_a/n_{0,a} = \pi^{-1/2}x_a\exp(-x_a^2)/\tau_{||a}$. The average energy of the removed particles is equal to $T_{\perp a} + m_a v_{cr}^2/2$ which represents the loss of perpendicular and parallel energy, respectively. Since $T_{\perp a} = T_{a,0}$ is unaffected by parallel losses, we obtain $\gamma_a = q_a/\Gamma_a T_{a,0} = 1 + x_a^2$.

The second method consists in differentiating (n/n0)a and $(\varepsilon/\varepsilon_0)_a$ obtained previously with respect to time, such that $2\Gamma_a = dn/dt = n_{0,a}d/dt(n/n_0)_a$ and $2q_a = dea/dt = \varepsilon_{0,a}d/dt(\varepsilon/\varepsilon_0)_a$. These derivatives can be evaluated using the chain rule $d/dt = (dx_a/dt)d/dx_a$ with $dx_a/dt = d/dt(\tau_{||a}/t) = -x_a 2/\tau_{||a} = -x_a/t$ and Leibnitz's formula for the derivative of a definite integral [3],

$$
\begin{aligned}
G_{\Gamma}^{\infty}(x_a) &= \left(\frac{\Gamma_a}{n_0}\right)_a = \frac{1}{2}\cdot\frac{dx_a}{dt}\cdot\frac{d}{dx_a}\left(\frac{n}{n_0}\right)_a = \frac{1}{\sqrt{\pi}}\cdot\frac{x_a e^{-x_a^2}}{\tau_{||a}}, \\
G_q(x_a) &= \left(\frac{q_a}{\varepsilon_0}\right)_a = \frac{1}{2}\cdot\frac{dx_a}{dt}\cdot\frac{d}{dx_a}\left(\frac{\varepsilon}{\varepsilon_0}\right)_a = \frac{1}{\sqrt{\pi}}\cdot\frac{\frac{2}{3}(1 + x_a^2)\, x_a^2\, e^{-x_a}}{\tau_{||a}} \\
\therefore \gamma_a^{\infty} &\equiv \frac{q_a^{\infty}}{\Gamma_a T_{a,0}} = 1 + x_a^2
\end{aligned}
\qquad (4.10)
$$

in exact agreement with the results obtained using the first method. The above expressions are shown graphically in Fig.4.2. The particle deposition rate reaches a maximum of $\Gamma_a^{max} \approx 0.207/\tau_{||a}$ at the thermal velocity, $x_a = 1$, while the energy deposition rate reaches a maximum of $q_a^{max} \approx 0.474/\tau_{||a}$ at $x_a = 1.27$. Consequently, the energy flux peaks earlier, t = 0.79t||a than the particle flux, $t = \tau_{||a}$. The ratio ga is initially infinite, due to prompt loss of the energetic particles in the tail of the Maxwellian distribution, but decays to the steady-state value of $\gamma_a^{\infty} = 2$ in one thermal transit time $t = \tau_{||a}$, at which v_{cr} reaches the thermal speed, $x_a = 1$. Afterwards, only sub-thermal particles are lost and γ_a decays asymptotically to unity, Fig.4.3. To quantify the degree of supra-thermal effects it is useful to define the parallel Mach number as v_{cr} normalised to the parallel thermal speed at time t, such that $M_{||a}$ is positive definite

$$
M_{||a} \equiv \frac{v_{cr}}{v_{Ta}(t)} = \frac{v_{cr}}{\int_{-\infty}^{\infty}\int_{0}^{v_{cr}} v_{||} f_{M,a}(v_{||}, v_{\perp}) dv_{||} dv_{\perp} / n_0}\left(\frac{T_{||}}{T_0}\right)_a^{\frac{1}{2}} \ddagger 1 \qquad (4.11)
$$

With this definition $M_{||a}$ behaves similarly to γ_a (infinite at t = 0, unity at $t \to \infty$), but decays much quicker in the initial phase, reaching a value of ~1.4 at $x_a = 1$, Fig.4.3.

The above results can also be expressed in terms of characteristic loss times for density and energy,

$\tau_{n,a}$ and $\tau_{\varepsilon,a}$, which can be useful in the fluid formulation,

$$\Gamma_a = \frac{n_a}{2} \equiv \frac{n_a}{\tau_{n,a}}, \qquad \therefore \frac{\tau_{n,a}}{\tau_{\|a}} = \sqrt{\pi}\, x_a e^{-x_a^2}$$
$$q_a = \frac{\varepsilon_a}{2} \equiv \frac{n_a}{\tau_{e,a}}, \qquad \therefore \frac{\tau_{\varepsilon,a}}{\tau_{\|a}} = \frac{\mathrm{erf}(x_a) - \frac{2}{3\sqrt{\pi}} x_a e^{-x_a^2}}{\frac{2}{3\sqrt{\pi}}(1 + x_a^2) x_a e^{-x_a^2}} \tag{4.12}$$

4.1.1 In-out divertor asymmetries

Having constructed a simple kinetic model based on the Maxwellian approximation, we next use it to address two important ELM-related problems: the in-out divertor asymmetry in the ELM power deposition, and the difference in electron and ion transient energy fluxes.

Since the initial Maxwellian distribution is even-symmetric and remains so in the absence of forces and collisions, the same number of particles and the same amount of energy must be deposited on either target, i.e. $\int\Gamma_o dt/\int\Gamma_i dt$ and $\int q_o dt/\int q_i dt$ must be equal to unity. According to (4.12), $\Gamma_a \propto \tau_{\|a}^{-1} \propto L_\|^{-1}$ so that this deposition occurs on a faster scale at the outer target (below we assume that s = 0 corresponds to the outer mid-plane and that $L_{\|i} > L_{\|o}$, as is the case in most large tokamaks, including JET and ITER). As a result, particles have less time to disperse in the outboard side of the filament and the arriving pulse is more intense at the outer target. This is illustrated in Fig.4.4 where Γ_a and q_a are plotted vs. $t/\tau_{\|a,o}$ for both targets assuming $L_{\|i}/L_{\|o} = 2$; here $\tau_{\|a,o} = L_{\|o}/\nu_{T,a}$ is the thermal transit time to the outer target. The transient pulse arrives earlier at the closer (outer) target, since $x_o/x_i = \tau_{\|o}/\tau_{\|i} = L_{\|o}/L_{\|i} = 1/2$, which leads to a compression of the pulse profile by a factor of two with respect to the inner target. The ratio of peak fluxes is inversely proportional to the ratio of connection lengths, $\Gamma_{a,o}^{max}/\Gamma_{a,i}^{max} = q_{a,o}^{max}/q_{a,i}^{max} = L_{\|i}/L_{\|o} = 2$.

The evolution of the in-out flux ratios is shown in Fig.4.5. The ratios $\Gamma_{a,o}/\Gamma_{a,i}$ and $q_{a,o}/q_{a,i}$ are infinite at t = 0, reach unity at $t/t\|a,o \sim 2$ and 1.5, respectively, and saturate at $L_{\|o}/L_{\|i} = 1/2$ for $t >> \tau_{\|a,o}$. The associated ratio of energy per particle γ_i/γ_e increases from $(L_{\|o}/L_{\|i})2 = 1/4$ at t = 0 to unity at $t >> \tau_{\|a,o}$, while $M_{\|o}/M_{\|i}$ changes from 0.5 to 1 in the same limits.

The decay of inner-to-outer filament ratios of density, energy and temperature is illustrated in Fig.4.6. All three are initially equal to unity, and while the density and energy ratios decay to $L_{\|o}/L_{\|i} = 1/2$ at $t >> \tau_{\|a,o}$, the temperature drops by 20% before approaching unity. In contrast, the parallel temperature ratio decays to $L_{\|o}/L_{\|i} = 1/2$ after $t \sim \tau_{\|a,o}$ and approaches $(L_{\|o}/L_{\|i})2 = 1/4$ for $\tau_{\|a,o} >> 1$. The outer filament is thus rarefied and its parallel energy effectively cooled by faster losses, although the net temperature of the whole filament remains roughly equal.

In light of the simplifying assumptions, it is perhaps surprising that the Maxwellian model can successfully reproduce the observed Type-I ELM delay between the outer and inner targets as measured on JET and other tokamaks. The observed delay is found to scale roughly as $\Delta_{tin\text{-}out} \sim (L_{\|i}/L_{\|o})/c_{s,ped}$, see Fig.13b of [55], which is entirely consistent with (4.12) and Fig.4.4. This agreement suggests that inertial effects alone are sufficient for determining the transient pulse arrival times. In contrast, Coulomb

forces become essential when calculating the magnitudes of the deposited fluxes, as will be shown in the following section.

4.1.2 Electron vs. ion transient energy fluxes

To compare the transient response of ions and electrons in a plasma filament, we once again focus on a single connection length $L_{||}$ and note that $x_i/x_e = \tau_{||i}/\tau_{||e} = v_{T,e}/v_{T,i} \sim (m_i/m_e\vartheta)^{1/2} \sim 60$ for D^+ ions with $\vartheta = T_{i,0}/T_{e,0} = 1$, which expresses the obvious fact that the lighter electrons are lost much faster than the heavier ions. In this context, the most serious shortcoming of the force-free Maxwellian model is the gross violation of charge neutrality in the plasma filament, $\Gamma_e/\Gamma_i >> 1$ and $n_e/n_i << 1$. This is illustrated in Fig.4.7 which shows the evolution of the ion to electron ratios of n, ε, T and $T_{||}$ plotted as function of $t/\tau_{||i}$. These ratios increase to values much larger than unity on the timescale of tlle, with ni/ne and ee/ei saturating at $(m_i/m_e\vartheta)^{1/2} \sim 60$ and $T_{||i}/T_{||e}$ at $m_i/m_e\vartheta \sim 3600$ for $t > \tau_{||i}$. The temperature ratio T_i/T_e rises to 3/2 and then decays back to unity on the timescales of $\tau_{||i}$ and $\tau_{||e}$, respectively. The ion and electron particle and energy fluxes on the divertor target are shown in Fig.4.8; they reach their maximum values at $t \sim \tau_{||e}$ and $\tau_{||i}$, respectively. The electron peak fluxes are larger by the ratio of thermal transit times, $\tau_{||i}/\tau_{||e} \sim 60$ such that the time integrated fluxes are equal (as they must be in the absence of forces and collisions). The ion to electron flux ratios, Γ_i/Γ_e and q_i/q_e, plotted in Fig.4.9, increase from zero at $t = 0$ to unity at $t/\tau_{||i} = 0.5$ and 0.4, respectively, and saturate at $(m_i/m_e\vartheta)^{1/2} \sim 60$ for $t > \tau_{||i}$. The associated gi/ge decreases from infinity at $t = 0$ to unity at $t >> \tau_{||a,o}$, never reaching the steady-state ratio obtained from kinetic analysis of the sheath problem, $\gamma_i^{\infty}/\gamma_e^{\infty} \sim 3/5$ [76]. This discrepancy is a direct consequence of the neglect of the Coulomb force in our simple model, which leads to the accumulation of positive charge density in the filament, ni/ne >> 1. In reality, this space charge would inhibit (augment) further electron (ion) losses, prevent further cooling of the electron channel and consequently reduce $T_{||i}/T_{||e}$.

To capture this effect within the Maxwellian model, we must strive to impose the quasi-neutrality constraint, $n_i \sim n_e$. However, a strict imposition of this constraint, $n_i = n_e$, At, leads to the trivial (and incorrect) result,

$$\frac{n_i}{n_e} = \frac{erf(x_i)}{erf(x_e)} = 1 \quad \Rightarrow \quad x_i = x_e \quad \Rightarrow \quad \frac{\varepsilon_i}{\varepsilon_e} = \frac{T_i}{T_e} = \frac{\Gamma_i}{\Gamma_e} = \frac{q_i}{q_e} = 1, \quad E_{||} = \nabla_{||}\varphi = 0 \tag{4.13}$$

in which the electron and ion species evolve in strict unison and the parallel electric field vanishes. In reality, we expect a violation of quasi-neutrality in the initial phase of the transient, when supra-thermal particles of both species are lost. A more accurate prescription would be to allow the electron and ion densities to evolve independently in the initial phase of the transient ($t << \tau_{||i}$), but require the re-establishment of quasi-neutrality on the timescale of the ion thermal transit time ($t > \tau_{||i}$). This weaker constraint may be imposed as a relation between x_i and x_e, reducing to the limiting values in the absence/presence of the quasi-neutrality constraint: $x_i/x_e \rightarrow (m_i/m_e\vartheta)1/2 \sim 60$ for $x_i >> 1$ and $x_i/x_e \rightarrow 1$ for $x_i << 1$. One possible functional form involves weighting the limiting values by the

transitional variable z(xi) which approaches zero and unity in the limits of small and large xi, respectively. This can be expressed as follows,

$$\frac{x_e}{x_i} = (1 - \zeta) + \zeta \left(\frac{m_e \vartheta}{m_i}\right), \qquad \zeta = \left(\frac{x_i}{1 + x_i}\right), \; y > 0 \tag{4.14}$$

where $y > 0$ is a free (fitting) parameter.

The effect of the weak quasi-neutrality constraint with $y = 1$ on the temporal evolution of particle and energy densities is shown in Fig.4.10. While both na and ea decay on the transit timescale t||a, such that the decay of ion quantities is delayed by $\tau_{||i} - \tau_{||e} \sim \tau_{||i}$, after this time the quasi-neutrality constraint (4.14) assures that all ion and electron quantities rapidly converge. The corresponding evolution of ion to electron thermodynamic ratios is shown in Fig.4.11. The effect of the delayed quasi-neutrality constraint is best appreciated by comparison with Fig.4.7. While n_i/n_e, ee/ei and $T_{||i}/T_{||e}$ exceed unity, they quickly ($t < \tau_{||i}$) saturate at 1.6, 2.6 and 3.6, respectively, a significant reduction from the unconstrained values of 60, 60 and 3600. The temperature ratio T_i/T_e rises by only 30%, before decreasing towards unity. The particle and energy fluxes on the divertor are shown in Fig.4.12 and should be compared with Fig.4.8. The electron fluxes are initially much larger, but converge to the ion fluxes, producing a quasi-ambipolar flow of charge for $t > \tau_{||i}$. The delayed quasi-neutrality constraint reduces the ratio of electron to ion peak particle and energy fluxes from 60, Fig.4.8, to 15 and 20, Fig.4.12. The ion to electron flux ratios, Gi/Ge and qi/qe, are plotted in Fig.4.13, which should be compared with Fig.4.9. In contrast to the monotonic increase in the absence of the quasi-neutrality constraint, both ratios reach their maximum values of 1.3 and 1.55 at $t/\tau_{||i} \sim 2$ and 1, respectively.

Comparison with measurements of Type-I ELM electron and ion pulse arrivals times at the divertor targets on JET and other tokamaks, eg. Fig.2.1 [51, 32], reveals that the weak quasi-neutrality Maxwellian model can successfully reproduce the observed delay between the electron and ion pulses. This delay is also observed in 1-D PiC simulations of ELM pulse propagation [9, 81]. Once again, we may conclude that inertial effects alone determine the ion and electron pulse arrival times at both divertor targets.

The asymptotic quasi-neutrality constraint ($n_i/n_e \rightarrow 1$ as $x_i \rightarrow 0$), also implies $\gamma_i/\gamma_e \rightarrow 1$, making it impossible to simultaneously satisfy both $n_i/n_e \sim 1$ and $\gamma_i/\gamma_e \sim \gamma_i^{\infty}/\gamma_e^{\infty} \sim 3/5$ in the Maxwellian approximation. This is perhaps not surprising, since the steady-state value originates with the pre-sheath electric field and the associated distortion of the ion distribution away from the shifted Maxwellian. Non-Maxwellian distributions, such as the variable skewness distributions used in turbulence theory to characterise intermittency [37], may therefore be required to satisfy both constraints. To overcome this shortcoming, the Maxwellian result $\gamma_a = 1 + x_a^2$ may be modified by a fitting parameter, eg. $\gamma_a = \gamma_{a,0} + x_a^2$. A more elegant approach would be to include the Coulomb force in the Vlasov equation, eg. $E_{||} = E_0 + 4\pi e(n_i - n_e)L_{||}$, such that each element $f_{M,a}(v_{||0}, v_{\perp 0})d\mathbf{v}$ is translated with changing velocity $v_{||a}(t) = v_{||0} + \int(e_a E_{||}/m_a)dt$, and arrives at $s_a(t) = \int v_{||a} dt$ after time t. The critical velocity $v_{||a}(t)$ and $x_a = v_{||a}(t)/v_{T,a}$ are then defined implicitly by $\{v_{||a}(t) \mid L_{||} = s(t)\}$. Since x_a depends

on n_a via $E_{||}$, the coupled system must be solved by numerical quadrature, i.e. by standard time marching algorithms which are both easy to implement and quick to execute. A more sophisticated (and expensive) solution, would involve abandoning the Maxwellian approximation altogether, and solving the 1D1V $(s,v_{||})$ Vlasov-Poisson system using a grid based finite-difference scheme. A number of public domain codes could be used for this purpose, many utilising specialised computational fluid dynamic (CFD) techniques [1]. The final step would consist in solving the complete 1D2V $(s,v_{||},v_{\perp})$ Fokker-Planck-Poisson system, with a simplified treatment of collisions, eg. using the BGK operator [11]. Numerical solutions of the complete system are discussed in the following section.

We may also consider the response of the Maxwellian model to a constant source, $\mathbf{S}_a = \delta(s)H(t)f_{M,a}(\mathbf{v})$, where H(t) is the Heaviside function. This will both illustrate the method of convolution, and permit a comparison with kinetic simulations, discussed in Section 4.2. As was already mentioned, the response to an arbitrary source can be obtained by integrating the Green's function responses to the delta function expansion of the source, as represented by the convolution formula (3.3). For example, the particle and energy fluxes on the target are found as

$$\Gamma_a(t) = \int_{-L_{||}}^{t} dt' \int_{-L_{||}}^{L_{||}} ds'\, G_{\Gamma,a}(s-s', t-t')\, S_a(r,t') = n_0 \int_0^t dt' \frac{1}{2}\frac{d}{dt'}\left(\frac{n}{n_0}\right)_a$$
$$\therefore \frac{\Gamma_a}{2n_0} = 1 - \left(\frac{n}{n_0}\right)_a = 1 - \mathrm{erf}(x_a), \quad \frac{q_a(t)}{n_0 T_{a,0}} = 1 - \left(\frac{\varepsilon}{\varepsilon_0}\right)_a = 1 - \mathrm{erf}(x_a) + \frac{2}{3\sqrt{\pi}} x_a e^{-x_a^2} \tag{4.15}$$

where the time integration of G_Γ and G_q yields G_n and G_e, respectively. The resulting fluxes are plotted in Fig.4.14, where the weak quasi-neutrality constraint has been assumed. As expected, both fluxes saturate at the value determined by the constant source for $t >> \tau_{||a}$, with the ratio ga approaching the half-Maxwellian effusion value of 2.

4.2 PARTICLE-IN-CELL SIMULATIONS

In the previous section, kinetic effects were derived from the simplest possible form of the Boltzmann equation, from which both forces and collisions were neglected. In order to assess the accuracy of these results, we would like to compare them with transient solutions of the full Fokker-Planck-Poisson system (4.1). Such solutions were recently obtained using the Particle-in-Cell (PiC) method in the context of ELM modelling [9]; a clear account of the PiC technique may be found in [13, 76]. Under low collisionality conditions, the PiC simulations confirm the underlying assumptions of the Maxwellian approximation, such as the constancy of $T_{\perp a}$ and uni-directional half-Maxwellian losses. The PiC simulations also indicate the arrival of electron and ion pulses on the scale of their respective transit times, eg. Fig.2 of [9], in good agreement with the predictions of Section 4.1.2. However, the Coulomb force is shown to increase (decrease) the ion (electron) energy arriving at the target. The ion to electron deposited energy ratio, $\int q_i dt / \int q_e dt$, not to be confused with ratio of energy densities in the filament τ_i/τ_e, was found to vary from 1 to 7 for a range of conditions, with values of ~3 being typical, see Table 1 of [9] (in the absence of the Coulomb force, this ratio is equal to unity as predicted by the half-Maxwellian loss model, Section 4.1.2).

The most accurate kinetic simulations of the ELM transient under JET relevant conditions have been performed using the BIT1 PiC code [80]. The improvements over previous simulations include a binary treatment of Coulomb collisions and much smaller shortening parameters [79]. The connection length $L_{||}/2$ was assumed as 40m in the simulation. In the pre-ELM phase, the upstream region was continuously supplied by a Maxwellian source with $T_e = T_i/2 = 100$eV, $n \approx 1\times10^{19}$ m^{-3}. The ELM was simulated by increasing this source to $T_e = T_i = 1500$eV, $n \approx 5\times10^{19}$ m^{-3} for a duration of 200μs (typical duration of a Type-I ELM on JET, see Fig.2.1). The length of the ELM pulse corresponds to $2.5\,\tau_{||i}$ evaluated with $L_{||o} \sim 30$m. However, the ELM source in the simulation was spatially distributed over nearly the entire SOL region above the X-point. The electron temperature, deposited energy flux and $\gamma_a = q_a/\Gamma_a T_a$, are shown in Fig.4.15 for the duration of the ELM pulse. Both γ_e and gi exhibit sharp peaks above their steady state values of $\gamma_e^{\infty} \sim 5$ and $\gamma_i^{\infty} \sim 3.5$, occurring at $t \sim \tau_{||e}$ and $\tau_{||i}$, respectively. The energy flux increases promptly ($t \sim \tau_{||e}$) due to electron loss, but reaches a plateau due to a repulsive electric field set up by the negative space charge. Only after the arrival of the bulk ion pulse at $t \sim \tau_{||i}$ does it increase further.

To compare the above PiC results with the predictions of the Maxwellian approximation, we have to combine the latter with the pre-ELM backbround, i.e. $\Gamma = \Gamma_{pre\text{-}ELM} + \Gamma_{ELM}$, etc. The pre-ELM fluxes are chosen in accordance with the PiC simulations ($n_{pre\text{-}ELM}/n_{ELM} \sim 0.2$, $T_{pre\text{-}ELM}/T_{ELM} \sim 0.1$, $\varepsilon_{pre\text{-}ELM}/\tau_{ELM} \sim 0.02$) and are shown in Fig.4.14. In order to calculate the Maxwellian response to a Heaviside source, $\mathbf{S}_a = \delta(s)H(t)f_{M,a}(\mathbf{v})$, a spatial convolution of the Green's function response is required. To approximate this effect, the ion transit time is chosen for the average connection length $(L_{||i} + L_{||o})/2 \sim 50$ m, such that $\tau_{||i} \sim 120$ms. To ensure correct asymptotic behaviour, $\gamma_e^{\infty} \sim 5$ and $\gamma_i^{\infty} \sim 3.5$ are assumed for the pre-ELM energy fluxes. The results are shown in Fig.4.16. It is clear that the Maxwellian approximation captures many of the features of the PiC simulations. The temporal scales are generally well reproduced, with the best match found for y = 1.7, which confirms the adapted choice of the weak quasi-neutrality constraint, (4.14). Although the peak ion value is well matched, gimax ~ 6.5, the peak electron value gemax ~ 35 is much larger in the PiC simulation. This discrepancy is a direct consequence of the neglected Coulomb force, and could be largely eliminated if the parallel electric field is included in the Vlasov system (see the discussion at the end of section 4.1.2).

5. FLUID DESCRIPTION OF PARALLEL LOSSES

In the previous section, we developed a model for the transient evolution of a collisionless plasma filament in contact with a solid surface. In order to include the effects of collisions, which become increasingly important as the filament cools, it is advantageous to construct an equivalent moment or fluid model, in which the effects of collisions are easily included via appropriate relaxation times [45]. This section is dedicated to the construction of such a model.

We begin by rewriting the set of moment equations (3.1) in the rest frame of the plasma filament and averaging over both perpendicular (⊥, ∧) directions (we suppress the subscript || on fluxes and velocities to simplify the notation),

$$
\begin{aligned}
&\frac{\partial n}{\partial t} + \nabla_{\|}\Gamma = S_n, && \Gamma \cong nu \\
&\frac{\partial \varepsilon_a}{\partial t} + \nabla_{\|}q_a = S_a = Q_{a,} && q_a = (\tfrac{1}{2}m_a u^2 = \tfrac{5}{2}T_a)\,\Gamma - n\,\chi_{\|a}\,\nabla_{\|}T_{\|} \\
&Q_a = \frac{\varepsilon_i - \varepsilon_e}{\omega_{ie}} = -Q_{i,} && \varepsilon_a = (\tfrac{1}{2}m_a u^2 = \tfrac{3}{2}T_a)n
\end{aligned}
\tag{5.1}
$$

We additionally assume no filament broadening (i.e. $D_{\perp} = D_{\wedge} = 0$), such that n and ea represent average density and energy in the filament; to simplify the analysis, we will treat filament broadening (i.e. finite $D_{\perp}$ and $D_{\wedge}$) at a later stage by assuming polytropic expansion in the $\perp-\wedge$ plane, see section 6.1. With the above assumption, the average quantities, n and ε_a, are reduced only by parallel losses, see (3.6). In accordance with the neglect of the Coulomb force in the Maxwellian approximation of Section 4, we assume quasi-neutrality to hold at all times, such that $n = n_e = Zn_i$ and $\Gamma = \Gamma_e = Z\Gamma_i$. To remove the final spatial dimension, we replace the parallel gradients by the inverse connection length, $\nabla_{\|} \rightarrow L_{\|}^{-1}$, obtaining the 0-D model equations,

$$
\begin{aligned}
&\left(\frac{\partial}{\partial t} + \frac{1}{\tau_n}\right) n = S_n, \\
&\left(\frac{\partial}{\partial t} + \frac{1}{\tau_{\varepsilon,i}}\right) \varepsilon_i + \frac{\varepsilon_i - \varepsilon_e}{\omega_{ie}} + s_i \\
&\left(\frac{\partial}{\partial t} + \frac{1}{\tau_{\varepsilon,e}}\right) \varepsilon_e - \frac{\varepsilon_i - \varepsilon_e}{\omega_{ie}} + s_e
\end{aligned}
\tag{5.2}
$$

where n and ε_a now represent averages over the whole filament, and the associated loss times are given by

$$
\begin{aligned}
&\tau_n \sim \frac{L_{\|}}{u} \sim \frac{L_{\|}}{Mc_s} \sim \frac{L_{\|}}{M\xi v_{ti}} \qquad \tau_{x,a} = \frac{5}{2} \cdot \frac{L_{\|}^2}{\chi_{\|a}} \\
&\tau_{\varepsilon,a} = \frac{3}{5}\,(\tau_n^{-1} + \tau_{\chi,a}^{-1})^{-1} = (\tau_n^{-1} + \tau_{Ta}^{-1})^{-1}
\end{aligned}
\tag{5.3}
$$

The second line of (5.3) defines the temperature decay time $\tau_{T,a}$ in terms of $\tau_{e,a}$ and τ_n, which follows from $\varepsilon_a \sim 3/2 \times nT_a$ where the filament averaged compressional energy, $1/2 \times nm_a u^2$ was assumed to be small. In (5.3), M is the parallel Mach number with respect to the sound speed, $c_s = [(ZT_e + T_i)/m_i]^{1/2} = (1 + Z/\vartheta)^{1/2} v_{ti} = \xi v_{ti}$, Z is the ion charge, $v_{ti} = (T_i/m_i)^{1/2}$ is the characteristic thermal ion speed and $\vartheta \equiv T_i/T_e$. The parallel heat conductivities are given by the harmonic averaged, heat flux limited expressions,

$$
\begin{aligned}
&\chi_{\|a} = \chi_{\|a}^{SH} / (1 + \Omega_{a\chi}), \quad \chi_{\|a}^{SH} = c_{\|a} v_{ta} \lambda_{aa}\,, \quad c_{\|i} = 3.9, \;\; c_{\|e} = 3.2 \\
&\Omega_{a\chi} = (c_{\|a}/\alpha_a)(v_{ta}\tau_{aa})(\nabla_{\|}T_a/T_a) \sim (c_{\|a}/\alpha_a)(\lambda_{aa}/L_{\|}) \sim c_{\|a}/\alpha_a \nu^*_a
\end{aligned}
\tag{5.4}
$$

where $\chi_{\|a}^{SH}$ are the classical Spitzer-Harm-Braginskii heat diffusivities [74, 18, 5], $\nu_a^* \equiv L_{\|}/\lambda_{aa}$

= $L_{\|}$/vtataa the collisionalities and $\alpha_a = q_a/nT_a v_{t,a}$ the flux limiting factors, otherwise known as the free streaming multipliers, i.e. the ratio of the actual flux to the free streaming value [75]. Equations (5.2) – (5.4) constitute a closed model with three specified time-independent parameters (the system size $L_{\|}$, the atomic mass A, and the ion charge Z), and three free parameters (M, α_i and α_e), which may vary with time.

The model equations (5.2) – (5.4) may be written in dimensionless form as

$$\begin{aligned}
&\left(\frac{\partial}{\partial t} + \frac{\tau_{n,0}}{\tau_n}\right) n = S_n, && t' = \frac{n}{\tau_{n,0}}, \quad n' = \frac{n}{n_0}, \quad s_n' = \frac{s_n \tau_{n,0}}{n_0} \\
&\left(\frac{\partial}{\partial t'} + \frac{\tau_{n,0}}{\tau_{\varepsilon,i}}\right) \varepsilon_i' + \left(\frac{\tau_{n,0}}{\tau_{\varepsilon,i}}\right)\left(\varepsilon_i' - \varepsilon_e'\right) |= s_i' && \varepsilon_i' = \frac{\varepsilon_i}{\varepsilon_{i,0}}, \quad s_i' = \frac{s_i \tau_{n,0}}{\varepsilon_{i,0}} \\
&\left(\frac{\partial}{\partial t'} + \frac{\tau_{n,0}}{\tau_{\varepsilon,e}}\right) \varepsilon_e' - \left(\frac{\tau_{n,0}}{\tau_{ie}}\right)\left(\varepsilon_i' - \varepsilon_e'\right) |= s_e' && \varepsilon_e' = \frac{\varepsilon_e}{\varepsilon_{e,0}}, \quad s_e' = \frac{s_e \tau_{n,0}}{\varepsilon_{e,0}}
\end{aligned} \tag{5.5}$$

where time has been normalised by the particle loss time evaluated at the initial conditions, $\tau_{n,0}$. Aside from the sources, they depend on three dimensionless ratios: $\{\tau_{\varepsilon,i}, \tau_{\varepsilon,e}, \tau_{ie}\}/\tau_n$. The functional form of these times may be found in Appendix A of [30]. As expected, the normalised time ratios can be reduced to a combination of only two dimensionless plasma parameters, namely ν_e^* and ν_i^*, or alternatively ν_e^* and ϑ. The reason for this reduction can be traced to the fact that the Fokker-Planck and Maxwell's equations which underlie all dynamical plasma equations, including the Braginskii equations which form the starting point of our fluid model (5.1), depend on four dimensionless parameters (for given values of A and Z), typically chosen as ρ^*, ν_e^*, β and ϑ. Since both ρ^* and β depend on the magnetic field, while parallel dynamics do not, we expect (5.1) to depend only on ν_e^* and J. Consequently, the homogenous (source-free) part of the solution is completely determined by the initial values, ne,0* and J0 in addition to the ion mass and charge.

$$\left\{n', \varepsilon_i', \varepsilon_e'\right\} = F\left(t'; \upsilon_{e,0}, \vartheta_0.A,Z\right) \tag{5.6}$$

Equations (5.5) thus form an initial value problem which can be solved numerically for specified, $\nu_{e,0}^*$ and ϑ_0 and sources, S_n', S_i', S_e'(t). Since an initial value problem is inherently transient (aside from the trivial case when the system is in steady state), it is not necessary to introduce the perturbation via the sources. In order to maximise the transient response, all sources were therefore set to zero (it should be stressed that inclusion of arbitrary sources does not complicate the solution of the problem, although the sources may depend non-linearly on the solution); as a result, density and energy decay to zero as $t \to \infty$. The system was solved by a forward marching numerical quadrature using a 4^{th} order Runge-Kutta method [3].

As an example, we choose for initial values the typical JET pedestal conditions: $n_0 = 10^{20}\ m^{-3}$, $T_{e,0} = T_{i,0} = 1keV$, with $L_{\|} \sim 30m$ as appropriate for $q_{95} \sim 2.7$. In Fig.5.1, the characteristic times for

these values of n_0, T_0 and $L_{||}$ are plotted in the ELM relevant temperature range of 10–1000eV (the Bohm criterion, M = 1, was used to specify the Mach number, while ai and ae were chosen such that $\gamma_e \rightarrow \gamma_e^{\infty} \sim 5$ and $\gamma_i \rightarrow \gamma_i^{\infty} \sim 3.5$ in the collisionless limit, $\nu_e^* \rightarrow 0$, see Section 5.2 below). The same information, presented in dimensionless form, is shown in Fig.5.2, where the normalised times are plotted vs. the electron collisionality. Also shown in both figures are the ion-ion and electron-electron collision times, at which the respective plasma species relax to a Maxwellian distribution; these times are shorter than tie by the square root of the mass ratio, $\tau_{ie}: \tau_{ii}: \tau_{ee} \sim 1: (m_e/m_i)^{1/2}: m_e/m_i$, justifying the two-fluid approach. The collisional times tend to increase with temperature, in contrast to the transport times which decrease with $T_i = T_e$. It is useful to list the ELM filament temperatures at which the particular times are equal to 100 ms; recall that transit times for typical JET Type-I ELMs lie in the range 100–200μs. Consulting Fig.5.1 these temperatures are found as:

- $T_i = T_e \sim 1000$eV for $\tau_n = 100\mu$s,
- $T_i = T_e \sim 500$eV for $\tau_{T,i} = 100\mu$s,
- $T_i = T_e \sim 250$eV for $\tau_{e,i} = 100\mu$s,
- $T_i = T_e \sim 150$eV for $\tau_{T,e} = 100\mu$s,
- $T_i = T_e \sim 100$eV for $\tau_{e,e} = 100\mu$s,
- $T_i = T_e \sim 45$eV for $\tau_{ie} = 100\mu$s.

In addition, the normalised times $\{\tau_{T,i}, \tau_{T,e}, \tau_{ie}\}/\tau_n$ are equal to unity at $T_i = T_e \sim 300$, 40 and 100eV and ne* ~ 5, 250 and 40, respectively. In other words, the ion temperature decays faster than the density for $T_i > 300$eV or $\nu_i^* < 5$, while the same is true of the electron temperature for $T_e > 40$eV or $\nu_e^* < 250$. In contrast, the ion-electron equilibration rate is faster than the density decay rate for $T_e <$ 100eV or $\nu_e^* > 40$. We therefore expect a hot (1keV) filament to cool faster than it dilutes, with electrons cooling faster than the ions. When Te reaches ~ 100eV, the ions should become additionally cooled by collisions with the already much colder electrons, and the two temperatures should begin to converge. This behaviour will indeed be observed in the numerical solutions of (5.5) presented in Sections 5.1-5.3.

Finally, we need a criterion for comparing the fluid and kinetic solutions, for which we choose the sheath energy transmission coefficient, $\gamma_a = q_a/T_aG$. Capturing the correct temporal evolution of ge and gi as indicated by the kinetic results of Section 4.2, eg. Fig.4.15, is a key requirement of any simple transient parallel loss model of magnetised plasma bounded by solid surfaces (open field line response). This criterion can therefore be used to evaluate the performance of a fluid model and eventually normalise the results in terms of several fitting parameters. The intention would be to merge the fluid and kinetic models into a simple kinetic-fluid hybrid. In the rest of this section, we investigate the validity of this project in order of increasing complexity.

We begin by solving the model equations for two ion species, D^+ (A = 2, Z = 1) and He^{++} (A = 4,

Z = 2) with initial temperatures of $T_{e,0} = T_{i,0} = 1$keV and for two values of the initial density, $n_0 = 10^{19}$ m^{-3} and 10^{20} m^{-3}. With these temperatures, $\tau_{n,0} = L_{\|}/c_{s,0}$ is equal to 67, 95 and 134 ms for H^+, D^+ and He^{++}, respectively. In Sections 5.1-5.3, we discuss the solutions with different assumptions on the free model parameters: M, α_i and α_e (or alternatively, γ_e and γ_i).

5.1 SHEATH LIMITED REGIME: M=1, $\gamma_e = \gamma_e^\infty$, $\gamma_i = \gamma_i^\infty$

The simplest fluid case is the so called sheath limited regime, defined by the Bohm criterion, M = 1, and the energy fluxes, $q_a = \gamma_a^\infty T_a \Gamma$ with $\gamma_e^\infty \sim 5$ and $\gamma_i^\infty \sim 3.5$, and n and Ta constant along the filament; it is generally valid at low collisionality under steady state conditions [75]. The constraints on the energy fluxes can be implemented directly into the code in place of the definition of q_a found in (5.1), which is equivalent to choosing the free streaming multipliers as $\alpha_i >> 1$, $\alpha_e = 2.5\xi(v_{ti}/v_{te})$. Solving the system, we find an exponential decay of n, T_i and T_e and a monotonic growth of T_i/T_e. With the chosen initial conditions, the filament becomes collisional at t' ~ 1 or t ~ 100μs. Both ge and gi remain constant at the imposed steady-state values, in contrasts to the kinetic results, Fig.4.15. We can therefore dismiss the sheath limited model as invalid for plasma energy transients, except in situations in which the steady state values, M=1, $\gamma_e = \gamma_e^\infty$, $\gamma_i = \gamma_i^\infty$ can be assumed to hold at all times. Ironically, this is only expected at the high collisionality, which contradicts the other sheath limited regime assumption, namely $n \sim T_a \sim$ const. In the following sections, we investigate the effect of parallel dynamics on the filament evolution.

5.2 PARALLEL DYNAMICS WITH THE BOHM CRITERION: M=1, $\alpha_i = 3.5\xi$, $\alpha_i = 5\xi(v_{ti}/v_{te})$

To allow γ_i and γ_e to evolve in response to the parallel plasma dynamics, we next consider the case in which the Bohm criterion is imposed at all times, but the energy densities evolve according to (5.2)-(5.4). This is equivalent to choosing the flux limiting factors as $\alpha_i = 3.5x$ and $\alpha_e = 5\xi(v_{ti}/v_{te})$, so that $\gamma_e \rightarrow \gamma_e^\infty = 5$ and $\gamma_i \rightarrow \gamma_i^\infty = 3.5$ in the low collisionality limit (the same values were used for Fig.5.1). The resulting decay of $n' \equiv n/n_0$, $T_i' \equiv T_i/T_{i,0}$ and $T_e' \equiv T_e/T_{e,0}$ is shown in Fig.5.3 for D^+ ions at the two different initial densities. As predicted earlier based on Fig.5.1, both temperatures decay faster than the density, and rapidly converge after t' ~ 2–3 or t ~ 200–300μs for the high density case, and t' ~ 3–5 or t ~ 300–500μs in the high density case (as expected due to lower collisionality). Since the deposited fluxes can be obtained as, $\Gamma' \sim dn'/dt$ and $q_a' \sim d\varepsilon a'/dt$, these are maximum at t = 0 and decay exponentially with time. The ratio T_i/T_e shown in Fig.5.4, reaches a maximum of ~ 2.5–3 for D and ~ 3.5–5 for He at t' ~ 1 – 1.5 for high density and t' ~ 2–2.5 for low density. The γ_i and γ_e for the D cases are plotted in Fig.5.5. They decay from their initial values of gi ~ 5–6 and $\gamma_e \sim 7.5$ to the asymptotic limit of ~ 3. Although the peak values are too low compared with Fig.4.15, the ratio γ_i/γ_e, is in better agreement, with $\gamma_i/\gamma_e > 1$ for t' > 1.5–2.5.

5.3 PARALLEL DYNAMICS WITH DELAYED BOHM CRITERION: M = Ψ(t'–1), $\alpha_i = 3.5M\xi$, $\alpha_e = 5\xi(v_{ti}/v_{te})$

Kinetic analysis presented in Section 3, suggests that transient losses are delayed by roughly one transit time to the nearest solid surface, as illustrated in Fig.4.1 or, for both ions and electrons, in Fig.4.10. A comparison of the latter with Fig.5.3 shows the absence of this behaviour in the fluid results of Section 5.2. This can be traced to the M = 1 assumption, which overestimates the ion loss in the initial phase of the transient. To introduce a delayed response we switch on the Bohm criterion only for $t' > 1$ or $t > \tau_{n,0}$, which is accomplished by setting $M = \Psi(t' - 1)$, where is $\Psi(t)$ a softer version of the Heaviside function, based on the hyperbolic tangent. Otherwise, we retain the ai and ae values of Section 5.2, i.e. $\alpha_i = 3.5M\xi$ and $\alpha_e = 5M\xi(v_{ti}/v_{te})$, which are now likewise delayed by $\Psi(t' - 1)$. The results, not shown here, indicate that all quantities, including the times of the peak temperature ratios, are indeed delayed by $\Delta t' \sim 1$ or $\Delta t \sim \tau_{n,0}$ (the peak temperature ratios themselves are largely unaffected by this delay). The initial values of γ_i and γ_e are ~ 6 and ~ 8, respectively, and decay to 4 and 3 after $t' \sim 2$, not unlike the half-Maxwellian results in Fig.4.16. Comparison with PiC simulations, Fig.4.15, suggests that the delay of the electron heat pulse should be removed in order to allow ge to transiently increase to values of order 10–100.

This may be implemented by removing the Mach number from the electron free streaming multiplier, $\alpha_e = 5\xi\xi(v_{ti}/v_{te})$, and otherwise retaining all assumptions of Section 5.3. The resulting decay of n', T_i' and T_e', shown in Fig.5.6, demonstrate that this combination is indeed closest to the kinetic results of Section 4.2, cf. Fig.4.10. The electron temperature now decays much faster than either the ion temperature or the density, although T_i' and T_e' still converge for long times, $t' >> 1$. Whereas the deposited electron energy flux, $q_e' \sim d\varepsilon_e'/dt$, still decays nearly exponentially with time, the plasma flux and ion energy fluxes now reach a maximum at roughly $t' \sim 1$. The ratio T_i/T_e shown in Fig.5.7 reaches a maximum value of ~ 3.5–4 for high density at $t' \sim 1.5–2$ and ~ 5–6 for low density at $t' \sim 1–1.5$. Finally, the gi and ge, plotted in Fig.5.8 for D^+ only, now tend to resemble the kinetic results of Fig.4.15, with ge decaying exponentially from very large initial values ~ 100 and gi from the moderate level of ~6; both variables saturate at ~3–4 for $t' >> 1$. Considering the crudeness of the imposed functional form of the delays and the moderate levels of collisionality in the fluid results, the agreement in the observed behaviour is encouraging. It suggests that given proper optimisation of the delay function, the essential features of the kinetic results could be captured in the moment approach.

One obvious improvement would consist of relaxing the quasi-neutrality constraint along the lines considered near the end of Section 4.1.2. This requires solving two density equations for ne and ni, coupled by the parallel electric field, $E_{||} \sim E_0 + 4\pi e(n_i - n_e)L_{||}$. This field must also be included in the energy equations as the work done on a moving charge $Q_{||,e} = -Q_{||,e} \sim eE_{||}\Gamma$, analogous to the energy equipartition term $Q_e = -Q_i$. The final system of four coupled equations should produce the desired delay due to the rise and fall of the space charge electric field.

6. APPLICATIONS OF THE PARALLEL LOSS MODEL

The development of the parallel loss model was largely motivated by experimental measurements of tokamak energy transients, primarily ELMs and disruptions. In this section we compare the model

against measurements of ELM filament fluxes and energies in the far-SOL of JET, and use this experience to predict the degree of ELM-limiter interaction on ITER. Since the ELM filaments in the JET experiments are initially semi-collisional ($n^* \sim 0.2 - 1$ evaluated with the mid-pedestal quanties), we restrict the comparison to the fluid approach.

6.1 COMPARISON WITH LIMITER PROBE MEASUREMENTS OF ELM FILAMENT DENSITIES AND ELECTRON ENERGIES ON JET

The degree of ELM-limiter interaction on JET was recently investigated [30]. The peak Type-I ELM filament densities and electron temperatures at the limiter location were measured using an array of Langmuir probes embedded in the outer poloidal limiters. The experiments were performed in deuterium plasmas (A = 2, Z = 1) with $B_\phi \sim 2.4$T, $I_p \sim 2.5$MA, $q_{95} \sim 2.7$, $P_{heat} \sim 10-16$MW, $\langle n_e \rangle / n_{GW} \sim 0.5 - 0.7$, $L_\parallel \sim 30$m and $f_{ELM} \sim 12-27$Hz. The nominal pedestal parameters were measured as $T_{e,ped} \sim T_{i,ped} \sim 1300$eV and $n_{e,ped} \sim 2.5\times10^{19}$ m^{-3}. Assuming the ELM filaments originate in the pedestal region, their initial values may be defined as averages between the pedestal-top and the separatrix, $T_{e,0} = (T_{e,ped} + T_{e,sep}) / 2 \sim 750\text{eV} \sim T_{i,0}$ and $n_{e,0} = (n_{e,ped} + n_{e,sep}) / 2 \sim 2\times10^{19}$ m^{-3}, such that $\tau_{n,0} = L_\parallel / c_{s,0} \sim 112\mu$s and $\nu^*_0 \sim 0.15$.

The above transit time is applied in the normalisation, $t' = t/\tau_{n,0}$. To estimate the time delay (Δt) between the start of parallel losses (t = 0) and the contact with the limiter, we need to consider two unknowns: the first is the radial velocity of the ELM filament in the SOL, the second is the radial distance the ELM filament travels from t = 0. The average radial propagation velocity of Type-I ELM filaments in these plasmas was measured as 450–750m/s, with the velocity in the limiter shadow of ~ 900m/s [30]. The above range of velocities was well matched by predictions of a filament propagation model based on sheath resistivity and parallel losses [24, 30]; we will use this fact to extrapolate the above values to other JET experiments and to ITER, sections 6.2 and 6.3. In the present plasmas, we may take the nominal Type-I ELM filament velocity as $\langle v_{\perp,ELM} \rangle \sim 600 \pm 200$m/s. Note that $\langle v_{\perp,ELM} \rangle$ has been observed to scale with ELM size, such that small (Type-III) ELMs propagate slower than large (Type-I) ELMs, and consequently deposit a smaller fraction of their initial energy on the limiter tiles [72]. There remains some disagreement as to the variation of $v_{\perp,ELM}$ in the SOL, with deceleration reported from JET and DIII-D [70, 19] and acceleration from MAST and AUG [48].

The estimate of the distance the ELM filament travels from t = 0 is more problematic. It is not clear whether t = 0 occurs at the pedestal top (eg. via peeling or reconnection of flux tubes to the divertor) [73] or at the pre-ELM separatrix location by radial transport to the existing SOL plasma [82]. So while the nominal distance from the separatrix to the limiter was $r_{lim} - r_{sep} \sim 90$ mm-omp, where rsep and rlim are the separatrix and limiter radii mapped to the outer mid-plane, the distance travelled by the ELM filament, $\Delta r = r_{lim} - r_0$, could range from rlim – r_{sep} to $r_{lim} - r_{ped}$. The pedestal width in these discharges was measured as ~ 30mm-omp, such that the possible radial range is $\Delta r \sim 90 - 120$ mm-omp. Combining the above yields $\Delta t = t_{lim} = \Delta r / \langle v_{\perp,ELM} \rangle \sim 150 - 200\mu$s and $t' \sim 1.33 - 1.78$.

We next solve (5.5) with A = 2, Z = 1 and the initial conditions corresponding to the mid-pedestal

values: 750eV and 2×10^{19} m^{-3}. To reduce the number of free parameters, we adopt the assumptions of Section 5.2, i.e. $M = 1$, $\alpha_i = 3.5\xi$, $\alpha_e = 5\xi(v_{ti}/v_{te})$, which correspond to the most rapid decay of all filament quantities. For the mid-pedestal time, $t' \sim 1.55$, we obtain the following average filament values at the limiter location,

$$n' \sim 0.44, \qquad T_i' \sim 0.185, \qquad T_e' \sim 0.063, \qquad W' \sim 0.055 \tag{6.1}$$

where $W' = n'(T_e'+T_i')/2$ is the normalised, average energy of the filament. We thus expect most ($1 - W' \sim 0.95$) of the ELM energy to be deposited at the divertor targerts, as is indeed inferred from power balance measurements in these high clearance discharges [56]. It is useful to express the above values in terms of effective exponential e-folding times $\tau_n/\tau_{n0} \equiv - t'/\ln n'(t')$, etc. and e-folding lengths, $\lambda_n = \langle v_{\perp,ELM}\rangle\tau_n$, etc.,

$$\begin{aligned} &\tau_n/\tau_{n0} \sim 1.89, \quad \tau_{Ti}/\tau_{n0} \sim 0.91, \quad \tau_{Te}/\tau_{n0} \sim 0.56, \quad \tau_W/\tau_{n0} \sim 0.53 \\ &\lambda_n \sim 127\text{mm}, \quad \lambda_{Ti} \sim 61\text{mm}, \quad \lambda_{Te} \sim 37.5\ \text{mm}, \quad \lambda_W \sim 36\ \text{mm} \end{aligned} \tag{6.2}$$

Recalling the discussion in Section 3, we note that all the quantities in (5.8) are filament average values, which in the assumed absence of filament broadening ($D_\perp = D_\wedge = 0$) are reduced only by parallel losses. In order to compare the above predictions with the limiter probe measurements, we need to relate these average values to maximum values within the filament. In other words, we need to estimate the amount of filament broadening, or expansion, in the $\perp$–$\wedge$ plane. Such broadening was indeed observed in the above JET experiments where the Type-I ELM filaments were seen to expand in the limiter shadow with an effective diffusivity of $D_\perp^{ELM} \sim 500m^2/s$; unfortunately, we have no reliable information on the filament broadening in the main SOL. It is important to stress that such broadening may involve the stretching, shearing and eventual break-up of an individual filament into progressively smaller filaments [12, 33].

In section 3, it was shown that the broadening of a delta function filament may be quantified by (3.5) and (3.6), which indicate that the ratio of the average to peak densities increases as $n/n_{max} = n'/n_{max}' = \lambda_{int} = (D_\perp t)^{1/2}$. Here λ_{int} is the integral width, which vanishes at $t = 0$ as it must for a delta function impulse. This singularity is absent in a real (spatially finite) wave-packet filament, which consists of a radial distribution of delta functions. Such a pulse would broaden more gradually, with the largest effect close to its boundary. Hence, the amount of filament expansion inferred from the Green's function analysis should be treated as an upper estimate. It is noteworthy that normalised to any given time, the increase of λ_{int} becomes independent of $D_\perp$. To summarise, we expect the ratio of peak to average filament densities to decay no faster than $t^{-1/2}$. In the absence of reliable experimental data, we are forced to resort to an additional assumption regarding the relation between the integral width, lint and the distance traveled by the filament, $r = \langle v_{\perp,ELM}\rangle t$. In the rest of this section, we assume these quantities to be linearly proportional,

$$n_{max}'/n' = 1/\lambda_{int}\,, \qquad \lambda_{int}/r = \lambda_{int}/\langle v_{\perp,ELM}\rangle t = \text{const} \tag{6.3}$$

which requires $D_\perp/u_\perp$ to increase linearly with r (such monotonic increase of $D_\perp$ in the SOL is frequently reported in the literature, eg. [75]). The above scaling roughly corresponds to the situation depicted in Fig.2.3 and Fig.3.1, although in the latter case the ratio $D_\perp/u_\perp$ was assumed to be constant. Provided the initial filament width is defined by the pedestal width, $\lambda_{int}(t = 0) \approx r_{sep} - r_{ped} = \Delta_{ped}$, we can use (6.3) to estimate the degree of filament broadening and the corresponding reduction in the relative peak density at $t = \tau_{lim}$ as

$$n_{max}'/n' = \lambda_{int}(0)/\lambda_{int}(t_{int}) = (r_{sep} - r_{ped})/(r_{lim} - r_{ped}) = \Delta_{ped}/(\Delta_{ped} + \Delta_{SOL}) \tag{6.4}$$

In the present case, we find nmax'/n' = 3 / (9 + 3) = 0.25.

The corresponding relative peak temperature reduction may be estimated in the limits of adiabatic ($\gamma = 5/3$) and isothermal ($\gamma = 1$) expansion. Recall that polytropic expansion can be expressed as $d(pn^{-\gamma})/dt = 0$ which for an ideal gas implies $T \propto n^{\gamma-1}$. Thus for adiabatic expansion (no perpendicular heat flow, $\chi_\perp = 0$) we get $T \propto n^{2/3}$, and with a factor of two expansion, T_{max}'/T' is reduced by ~ 1.6. For isothermal expansion (infinite perpendicular heat diffusivity, $\chi_\perp = \infty$), T_{max}'/T' remains constant. Since $\chi_{\perp i} >> \chi_{\perp e}$ we may expect the ions to be closer to the isothermal, and electron to the adiabatic, expansion limits. Assuming moderate heat conduction (g = 4/3) for both species and $n_{max}'/n' \sim 0.25$ at the limiter location, the predictions (6.1) and (6.2) for the filament average values yield the desired peak filament quantities,

$$\begin{array}{lll}
n_{max}' \sim 0.11, & T_{i,max}' \sim 0.115, & T_{e,max}' \sim 0.04 \\
n_{max} \sim 2.2\times10^{18}\ m^{-3}, & T_{i,max} \sim 86eV, & T_{e,max} \sim 30eV \\
\tau_{n,max}/\tau_{n0} \sim 0.70, & \tau_{Ti,max}/\tau_{n0} \sim 0.72, & \tau_{Te,max}/\tau_{n0} \sim 0.48 \\
\lambda_{n,max} \sim 47mm, & \lambda_{Ti,max} \sim 48mm, & \lambda_{Te,max} \sim 32.5mm
\end{array} \tag{6.5}$$

for which $\tau_{W,max}/\tau_{n0} \sim 0.325$ and $\lambda_{W,max} \sim 22$mm. The above predictions are in fair agreement with the nominal peak ELM filament densities and electron temperatures measured at the limiter, $n_{max} \sim 2.4\times10^{18}\ m^{-3}$ and $T_{e,max} \sim 25$eV [30]. The density estimate was obtained from nominal peak probe current of 70 mA, projected probe area of $3mm^2$ (which includes a factor of four erosion as calibrated against the reciprocating probe data [72]) and assumed ion to electron temperature ratio, $T_i/T_e \sim 3$. The temperature was obtained from fitting the current-voltage spectrum for a statistical sample of over 100 Type-I ELMs. Although Langmuir probes provide no information about ion energies, we see that this estimate of T_i/T_e is in good agreement with the model prediction, $T_i/T_e \sim 2.95$. In other words, the parallel loss model offers a self-consistent match to the JET limiter data. This suggests that the ELM filaments may originate in the mid-pedestal region, propagate radially at the average SOL velocity

predicted by the sheath-limited model and expand polytropically with moderate radial heat conduction, $\gamma \sim 4/3$. We will denote this combination of assumptions as the mid-pedestal approximation:

- Mid-pedestal initial filament quantities: $n_0 \sim (n_{sep} + n_{ped})/2$, $T_0 \sim (T_{sep} + T_{ped})/2$
- Mid-pedestal transit time: $r_0 = (r_{ped} + r_{sep})/2$, $\Delta t_0 = (r_{lim} - r_0)/\langle v_{\perp,ELM} \rangle$
- Polytropic expansion coefficient mid-way between adiabatic and isothermal limits, $\gamma_{mid} \sim (5/3 + 1) / 2 = 4/3$.

6.2 COMPARISON WITH RFA MEASUREMENTS OF ELM FILAMENT ION ENERGIES ON JET

The obvious shortcoming of the Langmuir probe measurements is the lack of ion temperature information. Recently, first data on ELM ion energies in the far-SOL has been obtained on JET using a Retarding Field Analyser (RFA) probe head mounted on a fast-scanning, reciprocating assembly [62]. In this section, we briefly compare these measurements with predictions of the parallel loss model; the details of the experiment and an extended discussion of the comparison may be found in [62].

The RFA experiments were performed in hydrogen plasmas (A = Z = 1) with $B_\phi \sim 1.2$ T, $I_p \sim 1.2$MA, $q_{95} \sim 3$, $P_{heat} \sim 7$MW, $\langle n_e \rangle / n_{GW} \sim 0.7$ and $W_{dia} \sim 1.1$MJ. The ELMs were frequent ($f_{ELM} \sim 60$Hz) but Type-I, with a stored energy drop of $\Delta W_{ELM}/W_{dia} \sim 4–5$ %. The RFA probe was located near the top of the machine, reciprocating into the far-SOL region just beyond the outer-wall protection limiter radius, $r_{RFA} < r_{lim}$. The relevant ELM data was collected with the RFA located at $r_{RFA} - r_{sep} \sim$ 35mm-omp (mapped to the outer mid-plane). Pedestal parameters were measured as $T_{e,ped} \sim T_{i,ped} \sim$ 400eV and $n_{ped} \sim 2.5\times10^{19}$ m^{-3} such that $W_{ped}/W_{dia} \sim 1/3$ and $\nu^*_{ped} \sim 0.6$, assuming $L_\parallel \sim 30$m. The initial mid-pedestal ELM filament values are found as $T_{e,0} = (T_{e,ped} + T_{e,sep}) / 2 \sim 300\text{eV} \sim T_{i,0}$ and $n_0 = (n_{ped} + n_{sep}) / 2 \sim (1.5 – 2)\times10^{19}$ m^{-3}, such that $t_{n,0} = L^\parallel / \chi_{s,0} \sim 125$ ms and $\nu^*_0 \sim 0.6$.

To estimate the average radial propagation velocity of Type-I ELM filaments in the SOL, we use the value of 600m/s measured in the experiments discussed in section 6.1, and apply the scaling predicted by the filament propagation model based on sheath resistivity and parallel losses [24, 30]. Based on this model, we expect the filament velocity to scale roughly with the sound speed, so it may be lower by the square root of the ratio of mid-pedestal temperatures and atomic masses (D^+ vs. H^+), i.e. $(750/300)^{1/2}\times(1/2)^{1/2} \sim 1.1$ in the RFA plasmas. We can therefore estimate the filament velocity in the RFA plasmas as $\langle v_{\perp,ELM} \rangle \sim 600 \pm 200$m/s, which roughly corresponds to the values found in the earlier experiments.

Based on magnetic reconstruction the distance from the separatrix to the RFA was estimated as $r_{RFA} - r_{sep} \sim$ 35mm-omp, while the pedestal width was measured as ~ 50mm-omp. Hence, the distance travelled by the ELM filament, $\Delta r = r_{RFA} - r_0$, could range from $r_{RFA} - r_{sep}$ to $r_{RFA} - r_{ped}$, with a possible radial range of $\Delta r \sim 35 – 85$mm-omp. Combining the above yields $\Delta t = t_{RFA} = \Delta r / \langle v_{\perp,ELM} \rangle \sim 65 – 130$ ms and $t' \sim 0.5 – 1.1$.

The fluid model equations (5.5) were solved with A = Z = 1 for a range of initial conditions centred on the mid-pedestal values of 300eV and 1.5×10^{19} m^{-3} and the assumptions of Section 5.2, i.e. M = 1, $\alpha_i = 3.5\xi$, $\alpha_e = 5\xi(v_{ti}/v_{te})$. The normalised results are shown in Fig.6.1. They were obtained with 300eV and 1.5×10^{19} m^{-3}, and exhibit little variation for factor of two changes in the initial conditions. In the expected range, t' ~ 0.5 – 1.1, which is represented by a shaded region in Fig.6.1, we obtain the following average filament values at the RFA location: n' ~ 0.7 – 0.5, T_i' ~ 0.55 – 0.33, T_e' ~ 0.3 – 0.17, with the ratio T_i/T_e ~ 2 – 2.5. The middle of this range t' ~ 0.8, which corresponds to the mid-pedestal approximation, yields the following prediction:

n' ~ 0.57,	Ti' ~ 0.405,	Te' ~ 0.177,	W' ~ 0.166	
τ_n/τ_{n0} ~ 1.42,	τ_{Ti}/τ_{n0} ~ 0.885,	τ_{Te}/τ_{n0} ~ 0.46,	τ_W/τ_{n0} ~ 0.445	(6.6)
λ_n ~ 107mm,	λ_{Ti} ~ 66mm,	λ_{Te} ~ 34.5mm,	λ_W ~ 32.3mm	

We thus expect ~ 15% of the ELM energy to be deposited on the limiter tiles. Recalling the discussion in Section 6.1, we can estimate the reduction in the relative peak density at $t = t_{RFA}$ due to radial filament broadening as $n_{max}'/n' > (r_{RFA} - r_{sep})/(r_{RFA} - r_{ped}) \sim 0.5$. Assuming polytropic expansion with $\gamma = 4/3$ yields the desired peak filament values,

n_{max}' ~ 0.285,	$T_{i,max}'$ ~ 0.32,	$T_{e,max}'$ ~ 0.14	
n_{max} ~ 4.3×10^{18} m^{-3},	$T_{i,max}$ ~ 96.5eV,	$T_{e,max}$ ~ 42eV	(6.7)
$\tau_{n,max}/\tau_{n0}$ ~ 0.64,	$\tau_{Ti,max}/\tau_{n0}$ ~ 0.70,	$\tau_{Te,max}/\tau_{n0}$ ~ 0.41	
$\lambda_{n,max}$ ~ 48mm,	$\lambda_{Ti,max}$ ~ 52mm,	$\lambda_{Te,max}$ ~ 30mm	

With these estimates, we are finally ready to attempt a comparison with the experiment. Fig.6.2 shows ion saturation current density (top plot) and the ion collector current (bottom plot) measured by the probe for a typical Type-I ELM. The former is measured at the entrance slit plate directly intersecting the SOL plasma, whilst the latter is due to ions that have surmounted the retarding potential of 400 V applied to an electrode inside the RFA cavity. Both currents are measured on the ion-side of the device, i.e. the side facing towards the outer mid-plane, and hence looking into the outer divertor. Details of RFA interpretation are discussed in [62]. The spikes in the probe signals correspond to individual ELM filaments sweeping toroidally past the probe location, in addition, sampling at MHz resolution indicates smaller structures within each filament [71, 62]. These are seen more clearly on the saturation current due to bandwidth broadening in the collector signal (the same effect means that peak values of the collector current could be larger by up to 50%) [62]. Assuming the ELM evolves with toroidal mode numbers ~ 10 (or rather that it ejects ~ 10 individual plasma filaments into the SOL), as expected from both MHD stability analysis and observations on JET and other machines [71, 7, 47, 26, 8], the temporal differences between the individual spikes in Fig.6.2 imply rapid braking of toroidal rotation of the filament in the SOL, $v_\phi^{ELM}(r = r_{RFA})/v_\phi^{ped} \sim 0.1$ [62]; conversely if we

assume $v_\phi^{ELM}(r = r_{RFA}) \sim v_\phi^{ped}$, then toroidal mode numbers of order unity are inferred, i.e. a single ELM filament passing the RFA probe many times. The lower rotation velocity is comparable to that obtained in the inter-ELM or L-mode far-SOL based on the toroidal component of the parallel Mach numbers measured using fast scanning (reciprocating) Langmuir probes [62, 51]. Although the mechanism of toroidal braking in the SOL has not been clearly identified, we expect particle and energy removal (either by parallel losses or by filament disintegration) to be accompanied by toroidal momentum loss from the rotating filaments. The situation is analogous to a hydrodynamic boundary layer in which viscous effects lead to rapid reduction of the ambient velocity [66]. In the case of the SOL, the divertor targets and the adjacent sheath (which define the stationary, laboratory frame of reference) play the role of the solid surface in the boundary layer problem. Clearly more experiments are needed to resolve this important point.

Also shown in Fig.6.2 are the slit and collector currents predicted by the parallel loss model and including an appropriate analytic description of the RFA function [61]. This prediction was based on Fig.6.1 with $t' \sim 0.5-1.1$ and filament expansion leading to $n_{max}'/n' \sim 0.5$ and $T_{max}'/T' \sim 0.5^{\gamma-1}$ at $t = t_{RFA}$. Three cases are shown:

- Mid-pedestal values (300eV, 1.5×10^{19} m^{-3}) with adiabatic expansion ($\gamma = 5/3$)
- Mid-pedestal values (300eV, 1.5×10^{19} m^{-3}) with isothermal expansion ($\gamma = 1$)
- Pedestal values (400eV, 2.5×10^{19} m^{-3}) with adiabatic expansion ($\gamma = 5/3$)

In each case, the upper and lower limits of the predictions are shown, which correspond to $t' \sim 0.5$ and $t' \sim 1.1$ in Fig.6.1, respectively. While a significant variation in the predicted values may be discerned, it is encouraging that best agreement with the measured slit and collector currents, indicated by the shaded regions in Fig.6.2, is found with the mid-pedestal approximation, defined at the end of section 6.1 (although it should be noted that adiabatic expansion from the pedestal top offers a comparable level of agreement). This finding reinforces the conclusions drawn in section 6.1, namely that ELM filaments originate in the mid-pedestal region, propagate radially at the average SOL velocity predicted by the sheath-limited model and expand polytropically with $\gamma \sim 4/3$.

6.3 PREDICTION OF ELM-LIMITER INTERACTION ON ITER

Taking confidence from the favourable comparison found with recent JET data, sections 6.1 and 6.2, we next apply the mid-pedestal approximation to predict the peak Type-I ELM filament densities and temperatures at the outboard limiter location in ITER. We begin by assuming reference ITER plasma parameters, see Table 2.1 [43, 4, 50]: $R_0 \sim 6.2$m, $a \sim 2$m, $q_{95} \sim 3.0$, $L_{||} \sim 60$m, $B_\phi \sim 5.3$T, $n_{e,ped} \sim 2n_{e,sep} \sim 6\times10^{19}$ m^{-3}, $T_{i,ped} \sim T_{e,ped} \sim 4$ keV, $T_{i,sep} \sim 2T_{e,sep} \sim 400$eV, which yield the mid-pedestal quantities, $n_0 \sim (n_{ped} + n_{sep}) / 2 \sim 4.5\times10^{19}$ m^{-3}, $T_{e,0} \sim T_{i,0} \sim (T_{ped} + T_{sep}) / 2 \sim 2$keV, $\nu^*_{i,0} \sim \nu^*_{e,0} \sim 0.08$ and a related particle loss time, $t_{n,0} \sim 140$ ms. The radial propagation velocity of the ELM filament may be estimated based on the parallel loss limit of the sheath resistive filament propagation model, which predicts the following scaling [24],

$$\left(\frac{v_\perp}{c_s}\right)_{||loss} \propto T^{1/3} B^{-2/3} R^{-2/3} q_{95}^{-1/3} \tag{6.8}$$

As reported in [32], this expression may be used to extrapolate the JET results to the ITER reference conditions. Below we improve on the earlier estimate. In the first instance, we find $(v_\perp/c_s)_{ped}^{ITER}/(v_\perp/c_s)_{ped}^{JET} \sim (4/1.5)^{1/3}(5.3/2.4)^{-2/3}(6.2/3)^{-2/3}(3/2.7)^{-1/3} \sim 0.5$. This allows us to predict the SOL average radial filament velocity in ITER as

$$v_\perp^{ITER} \approx \frac{(v_\perp/c_s)_{ped}^{ITER}}{(v_\perp/c_s)_{ped}^{JET}} \times \frac{c_s^{ITER}}{c_s^{JET}} \times v_\perp^{JET} \approx 0.8 \times v_\perp^{JET} \approx 300 - 600\,\frac{m}{s} \tag{6.9}$$

The mid-pedestal to limiter distance on ITER is estimated as $\Delta r_0 = (r_{ped} + r_{sep})/2 + |r_{sep} - r_{lim}| \sim 5/2 + 5cm \sim 7.5cm$, which gives a mid-pedestal transit time of $\Delta t_0 = \Delta r_0 / \langle v_{\perp,ELM} \rangle \sim 120-210ms$ or $t' \sim \Delta t_0/\tau_{n,0} \sim 0.85-1.5$.

We next solve (5.5) assuming a pure deuterium filament with initial ITER mid-pedestal values and the Bohm (Section 5.2) and delayed Bohm (Section 5.3) approximations. The former, as shown in Section 6.1, offers good agreement with recent JET experiments. It also corresponds to the highest expected parallel losses from the ELM filament, and hence constitutes the lowest (most optimistic) prediction of the amount of ELM energy deposited on the ITER limiters. The results are shown in Fig.6.3, where $t' \sim 0.85-1.5$ is indicated by the shaded region. In this range, Fig.6.3 predicts the following average filament values at the limiter radius:

$$n' \sim 0.58-0.45, \quad T_i' \sim 0.26-0.16, \quad T_e' \sim 0.12-0.06, \quad W' \sim 0.11-0.05 \tag{6.10}$$

which give $\nu^*_i \sim 0.5 - 1$, $\nu^*_e \sim 2-10$ and $T_i/T_e \sim 2-2.8$. Also shown in Fig.6.3, are the results of the delayed Bohm approximation of Section 5.3, which estimates the upper bound of the reduction in parallel losses due to kinetic effects associated with the ion inertia. These may be expected to play a role in the initial stages of filament evolution on account of the low mid-pedestal collisionality, $\nu^*_0 \sim 0.08$. As expected, the delayed Bohm results predict much smaller reduction in filament density and ion temperature at the limiter radius,

$$n' \sim 0.97-0.9, \quad T_i' \sim 0.9-0.7, \quad T_e' \sim 0.13-0.07, \quad W' \sim 0.5-0.35 \tag{6.11}$$

such that $T_i/T_e \sim 7-10$. It is instructive to compare the delayed Bohm results with the purely kinetic, Maxwellian predictions of Section 3. Thus Fig.4.10 yields the following estimates in the range $t' \sim 0.85-1.5$,

$$n_i' \sim 0.9-0.7, \quad n_e' \sim 0.55-0.45, \quad T_{||,i}' \sim 0.65-0.25, \quad T_{||,e}' \sim 0.15-0.1 \tag{6.12}$$

where $T_{||,i}/T_{||,e} \sim 2.5-3.5$. Comparing the density decay (~0.95 vs. ~0.6), indicates that the assumed

ion delay, $M = \Psi(t' - 1)$, $\alpha_i = 3.5M\Psi$, significantly overestimates the actual kinetic effect. On the other hand, the Maxwellian results of Fig.4.10 suffer from the neglect of inter-particle collisions, which manifests itself in the asymptotic behaviour of the net temperatures, $T_i' \sim T_e' \rightarrow 2/3$ as $t' \rightarrow \infty$. In the presence of collisions, isotropisation of the velocity distribution would assure that $T_{\|,\alpha}' \sim T_{\perp,a}' \sim T_\alpha'$ in the long time limit; to capture this effect, a solution of the Fokker-Planck equation with a simplified collision operator, eg. in the BGK form, would be necessary. Without resorting to such a calculation, our best estimate in the trans-collisional region consists of the Bohm approximation multiplied by a kinetic enhancement factor Ki of order unity, $1 < K_i < 2$, such that: $n' \rightarrow K_i n'$, $T_i' \rightarrow K_i T_i'$, $T_e' \rightarrow T_e'$ (note the electron temperature is not affected by ion inertial effects). Since $K_i = 1$ with the mid-pedestal approximation successfully reproduced JET RFA results, one would expect Ki to be heavily weighted towards unity. On the other hand, the ELMs measured by the RFA on JET were much more collisional than those expected on ITER, $\nu^*_{ped} \sim 0.6$ vs. $\nu^*_{ped} \sim 0.08$, such that kinetic corrections would have been substantially smaller. The above results are summarized in Table 6.1.

To find peak filament values at the limiter location, we assume a polytropic radial expansion with $\gamma \sim 4/3$ and $n_{max}'/n' \sim (r_{lim} - r_{ped})/(r_{lim} - r_{sep}) \sim 5\text{cm}/10\text{cm} \sim 0.5$. Note that filament expansion does not affect the fraction of ELM energy deposited on the limiter tiles, which is predicted as $W' \sim (0.11 - 0.05) \times K_i^2$ or with $K_i \sim 1$ at between 5 and 10%. For the peak filament quantities, the Bohm approximation yields,

$$\begin{aligned} &n'_{max} \sim (0.29 - 0.23) \times K_i, \quad T_{i.max}' \sim (0.21 - 0.13) \times K_i, \quad T_{e.max}' \sim 0.10 - 0.05 \\ &n_{max} \sim (1.3 - 1) \times K_i \times 10^{19}\ \text{m}^{-3}, \quad T_{i.max} \sim (420 - 260) \times K_i\ \text{eV}, \quad T_{e.max} \sim 200 - 100\text{eV} \end{aligned} \tag{6.13}$$

Assuming a toroidal mode number of the ELM in the range, $n_\phi \sim 10 - 20$, the maximum poloidal extent of a filament may be estimated as $2\pi a/n_\phi \sim 0.6 - 1.2$m or more accurately as a Gaussian shape with a half width of $\sim 0.3 - 0.6$m. Given a specific limiter geometry, one may then calculate (within the above accuracy) the spatial and temporal distribution of the deposited ELM energy.

Finally, let us consider the implications of the predicted temperature range $T_{i.max} \sim (420 - 260) \times K_i$ eV, $T_{e.max} \sim 200 - 100$eV for ITER, bearing in mind that more experiments are clearly needed to increase the confidence level of this prediction. It is well known that the ion impact energy onto a solid surface, such as a limiter, consists of the ion energy into the sheath, $\sim 2T_i$, and the energy drop across the sheath, which accelerates the ions by additional $\sim 3T_e$. If the predicted temperature values prove accurate, we may estimate the average impact energy of ELM ions striking the limiter as $\sim 2T_{i.max} + 3T_{e,max} \sim 2 \times (420 - 260) \times K_i + 3(200 - 100)\text{eV} \sim 1.4 - 0.8$keV, assuming $K_i = 1$. Since this estimate represents the most optimistic scenario, we may expect Type-I ELM ions to cause significant sputtering of ITER limiters, irrespective of whether these are made of beryllium or tungsten. In both cases the threshold for physical sputtering would be exceeded, eg. for tungsten this threshold is roughly ~200eV for impact by T^+ and D^+ ions.

As a final result, we present a comparison of nominal peak filament quantities at the limiter locations predicted using the parallel loss model for three large tokamaks: AUG, JET and ITER. Deuterium ions and the usual Bohm assumption (M = 1) were used for the calculation. The mid-pedestal approximation was adopted in each case with the following initial (mid-pedestal) values:

- AUG: $n_0 \sim 3\times10^{19}\ m^{-3}$, $T_{e,0} \sim T_{i,0} \sim 0.45$keV; $\langle v_\perp \rangle \sim 450$m/s, $r-r_0 \sim 50$mm
- JET: $n_0 \sim 3\times10^{19}\ m^{-3}$, $T_{e,0} \sim T_{i,0} \sim 0.8$ keV; $\langle v_\perp \rangle \sim 600$ m/s, $r-r_0 \sim 60$mm
- ITER: $n_0 \sim 4.5\times10^{19}\ m^{-3}$, $T_{e,0} \sim T_{i,0} \sim 2$ keV; $\langle v_\perp \rangle \sim 480$ m/s, $r-r_0 \sim 75$mm

The nominal JET and ITER values were already cited in the previous sections, eg. Table 2.1, while AUG values were adopted from [47]. Also listed are the average radial ELM filaments velocities and the expected mid-pedestal to limiter distances; in this case AUG values were obtained from [49]. The solution of (5.5) in each case indicates that ~90% of the initial ELM energy is deposited on the divertor targets, with the fraction arriving at the limiters being equal to W' ~ 8, 11 and 8% in AUG, JET and ITER, respectively. Assuming the filaments expand polytropically with $\gamma \sim 4/3$ and that $n_{max}'/n' \sim 0.5$ at the nominal limiter radii, as predicted for each device by (6.4), the peak filament quantities at the limiter location may be determined, Table 6.2. Also listed in Table 6.2 are the effective e-folding times and radial e-folding lengths, cf. (6.3). The predicted ELM temperatures at the limiter increase roughly linearly with machine size (factor of four variation from AUG to ITER), while the radial e-folding lengths are comparable on all three machines (with ~50% variation from AUG to ITER). Based on Table 6.2, the predicted peak ELM filament ion impact energies at the nominal limiter radii, $E_{imp,max} = 2T_{i.max} + 3T_{e,max}$, may be calculated as ~270eV, 590eV and 1120eV for AUG, JET and ITER, respectively. Since these results represent the most optimistic scenario, we expect the threshold for physical sputtering of tungsten by T^+ and D^+ ions (~200eV) to be only mildly exceeded by typical Type-I ELMs on AUG, but significantly exceeded by comparable ELMs on JET and ITER (assuming outer wall gaps consistent with the values of r – r0 used in the calculation, see above). The heat loads on the limiters associated with the thermal quench in disruptions represent an additional and largely separate concern.

As a concluding remark the authors would like to point out that the above predictions contain a number of uncertainties and should therefore be treated with caution. Although an attempt has been made throughout the discussion to indicate the main cause of uncertainties in the prediction, a full fledged error analysis was not performed. Therefore, the reader may wish to view the above predictions as tentative.

CONCLUSIONS

Although parallel energy transients can now be calculated by numerical solution of the coupled Fokker-Planck and Poisson equations, these simulations are computationally expensive and are available only for limited conditions, eg. only a handful of kinetic ELM simulations have appeared in the

literature. It is therefore highly desirable to develop simplified models, which could capture as many of the salient features of the kinetic simulations as possible, yet offer substantial savings in both cost and complexity. The accuracy of such models could then be optimised with the help of several fitting parameters, so as to best match the available kinetic simulations. The simple models could be used either as stand alone tools, eg. for interpreting diagnostic data following energetic transients such as ELMs, thermal quench of disruptions and to a lesser extent intermittent turbulent bursts, or as modules for 2-D fluid plasma transport codes.

For this purpose, two simple models of parallel energy transients have been developed and described here, one based on the kinetic, the other on the fluid approach. In both cases, several simplifying assumptions have been invoked in order to minimise the computational time of the solution, eg. the Coulomb force leading to the parallel electric field has been neglected.

In the kinetic approach, the force-free Vlasov equation is used to construct a collisionless model of transient particle and energy fluxes onto a solid surface. The results are obtained in terms of definite integrals over the Maxwellian distribution, which can be evaluated analytically in terms of exponential and error functions. The quasi-neutrality constraint is imposed gradually, using a delay on the scale of the ion thermal transit time (this has been largely confirmed by kinetic simulations). Despite these simplifications, most of the features of the numerical solution of Fokker-Plank-Poisson system (using the PiC code BIT1) under JET relevant Type-I ELM conditions are captured by the analytical model. The remaining differences are caused by the absence of the Coulomb force in the simple model. This force may be included at different levels of sophistication, from purely analytical, to forward time marching, to a 1D1V Vlasov solution. Based on the preliminary analysis presented in Section 4, we can anticipate that moderate extensions can lead to a reasonably accurate model of the collisionless phase of the transient.

The same problem is also tackled using the fluid or moment approach, in which the coupled density and energy equations, including ion-electron collisional energy exchange, are solved numerically using a forward marching scheme. In keeping with the collisionless case, the parallel electric field is neglected in the first approximation; in addition, strict quasi-neutrality is assumed at all times. Despite these restrictions, the key features of the kinetic results can be captured in the 0-D moment formulation by introducing a delay to ion fluxes of the order of the thermal transit time. The T_i/T_e ratio is found to peak at ~3–5 for a wide range of conditions. For longer times, T_i and T_e converge due to collisional relaxation. The fluid model can be significantly improved at little additional cost by evolving two density equations, coupled by a parallel electric field.

Finally, it should be possible to create a kinetic-fluid hybrid model, weighting the two models by the collisionality of the plasma filament. Such approaches are common in Knudsen regime gas dynamics, and have the advantage of guaranteeing the correct asymptotic behaviour in both the low and high collisionality regimes. Provided both the kinetic and fluid models are computationally light, the benefit of evolving both simultaneously would greatly outweigh the additional complexity introduced by the hybridisation.

The parallel loss model has been compared to recent JET measurements of far-SOL ELM filament densities and electron temperatures using the limiter Langmuir probes and ion energies using a Retarding Field Analyser (RFA) probe [63]. In each case, the experimental data is well reproduced using the fluid approach (expected to apply for the semi-collisional ELM filaments in the JET experiments) including the Bohm assumptions of Section 5.2 and the mid-pedestal approximation. The same approximation is then used to estimate the degree of ELM-limiter interaction on ITER. Under the most optimistic assumptions, we expect 10% of the ELM energy to be deposited on the ITER limiters with the following peak filament values: $n_{max} \sim (1.3-1) \times Ki \times 10^{19}\ m^{-3}$, $T_{i.max} \sim (420-260) \times K_i$ eV and $T_{e.max} \sim 200-100$eV, where $1 < K_i < 2$ measures the degree of kinetic corrections (best agreement on JET was found with $K_i \sim 1$). This leads to a peak ion impact energy of $\sim 1.4-0.8$ keV, in excess of the threshold for physical sputtering for both beryllium and tungsten. Although more experiments are clearly needed to increase the confidence level of the above predictions, it is hoped that the present contributions will help in advancing our understanding of tokamak plasma transients as a whole, and ELMs in particular.

ACKNOWLEDGEMENTS

This work was conducted under European Fusion Development Agreement and was partly funded by EURATOM and the United Kingdom Engineering and Physical Sciences Research Council. We would like to thank O.E.Garcia, A.Loarte, V. Naulin, J.Paley and D.Tskhakaya for helpful discussions and comments.

REFERENCES

[1]. J.D Anderson, Jr., Computational Fluid Dynamics, McGraw-Hill, New York (1995).
[2]. G.Y.Antar et al., Phys. Plasmas **8** (2001) 1612.
[3]. G.B.Arfken and H.J.Weber, Mathematical Methods for Physicists, 5th ed. Harcourt (2001).
[4]. R.Aymar et al., Plasma Phys. Control. Fusion **44** (2002) 519.
[5]. R.Balescu, Transport Process in Plasmas, North-Holland (1988).
[6]. M.Becoulet et al., Plasma Phys. Control. Fusion **44** (2002) A103.
[7]. M.Becoulet et al., Plasma Phys. Control. Fusion **45** (2003) A93.
[8]. M.Becoulet et al., J. Nucl. Mat., **337-339** (2005) 677.
[9]. A.Bergmann, Nuclear Fusion, **42** (2002) 1162.
[10]. B.Beyer et al., Plasma Phys. Control.. Fusion, **41** (1999) A757.
[11]. P.L. Bhatnagar, E.P.Cross, M.Krook, Phys.Rev. **95**, 511 (1954).
[12]. N.Bian et al., Phys. Plasmas, **10** (2003) 671.
[13]. C.K.Birdsall and A.B. Langdon, Plasma Physics via Computer Simulation, McGraw-Hill, New York (1985).
[14]. D.Biskamp, Nonlinear Magnetohydrodynamics, Cambridge U. Press (1993).

[15]. D.Biskamp, Magnetic Reconnection in Plasmas, Cambridge U. Press (2000).
[16]. D.Biskamp, Magnetohydrodynamic Turbulence, Cambridge U. Press (2003).
[17]. J. Boedo et al., J. Nucl. Mat., **337-339** (2005) 771.
[18]. V.I.Braginski, in M.A.Leontovich (ed.), Rev. of Plasma Physics, Consultants Bureau, New York, 1965
[19]. A.V.Chankin, J. Nucl. Mat., **241-243** (1997), 199.
[20]. S.Chapman, T.G.Cowling, Mathematical Theory of Non-uniform Gases, Cambridge (1958)
[21]. R.Chodura, in D.E.Post, R. Behirsch (eds.), Physics of Plasma-Wall Interactions in Controlled Fusion, Plenum Press (1984) 99.
[22]. G. Counsell et al., Plasma Phys. Control. Fusion, **44** (2002), 827.
[23]. S.Cowley et al., Plasma Phys. Control. Fusion, **45** (2003) A19.
[24]. D.A. D'Ippolito et al., Phys. Plasmas, **9** (2002) 222.
[25]. T.Eich et al., J. Nucl. Mat., **337-339** (2005) 669.
[26]. T.Eich et al., Plasma Phys. Control. Fusion, **47** (2005a) 815.
[27]. M.Endler et al., Plasma Phys. Control. Fusion, **47** (2005) 219.
[28]. G.Federici et al., Nuclear Fusion **41** (2001) 1967.
[29]. W.Fundamenski et al., Nuclear Fusion, **44** (2004) 20.
[30]. W.Fundamenski et al., Plasma Phys. Control. Fusion, **46** (2004a) 233.
[31]. W.Fundamenski et al., J. Nucl. Mat., **337-339** (2005) 305.
[32]. W.Fundamenski et al., Nuclear Fusion., in press (2005a).
[33]. O.E.Garcia et al.,†Phys.Rev.Lett. **92**, 154003 (2004).
[34]. Ph. Ghendrih et al., Nucl. Fusion **43** (2003) 1013.
[35]. T.I.Gombosi, Gaskinetic Theory, Cambridge (1994).
[36]. B.Goncalves et al., Plasma Phys. Control. Fusion, **45** (2003) 1627.
[37]. J.P.Graves et al, Plasma Phys. Control. Fusion, **47** (2005) L1.
[38]. P. Helander, D.J.Sigmar, Collisional transport in magnetized plasmas, Cambridge U. Press, Cambridge, UK (2002).
[39]. A.Herrmann et al., Fusion Energy 2004, Proc. 20th Int. Conf. Vilamoura, IAEA, Vienna (2004).
[40]. J.D.Huba, NRL Plasma Formulary, Naval Research Laboratory, Washington, DC (2002).
[41]. C.Hidalgo et al., J. Nucl. Mat., **313-316** (2003) 863.
[42]. J.Hugill, Phys. Contr. Fusion **42** (2000), R75.
[43]. ITER Physics Basis, Nuclear Fusion, **39** (1999), 2137-2664, ß4.2, ß4.3.6.1, ß4.4.
[44]. K.Itoh, S-I Itoh, A. Fukuyama, Transport and Structural Formation in Plasmas, IoP, Bristol (1999).
[45]. S.Ichimiru, Statistical Plasma Physics, Vol. 1, Adison-Wesley, New York (1992).
[46]. A.Kallenbach et al., J. Nucl. Mat., **337-339** (2005) 381.
[47]. A.Kirk et al, Plasma Phys. Control. Fusion **47** (2005) 315.
[48]. A.Kirk et al, submitted to Plasma Phys. Control. Fusion (2005a).

[49]. N.A. Krall, A.W.Trivelpiece, Principles of Plasma Physics, San Francisco Press (1980).
[50]. A.Kukushkin et al, Nuclear Fusion, **43** (2003) 942.
[51]. B.LaBombard et al., Nucl. Fusion **44** (2004) 1047.
[52]. M.A.Lieberman, in Handbook of Plasma Immersion, Ion Implantation and Deposition, ed.A.Anders, John Wiley & Sons, New York (2000) 29.
[53]. E.M.Lifshitz and L.P.Pitaevskii, Physical Kinetics, Pergamon, Oxford (1981).
[54]. A. Loarte et al., Plasma Phys. Control. Fusion **45** (2003) 1549.
[55]. A. Loarte et al., Phys. Plasmas **11** (2004) 2668.
[56]. G.F.Matthews et al., Nuclear Fusion, **43** (2003) 999.
[57]. K.Miyamoto, Plasma Physics for Nuclear Fusion, MIT Press, Boston (1987).
[58]. P.M.Morse and H.Feshbach, Methods of Theoretical Physics, McGraw-Hill, New York (1953).
[59]. V.Naulin, et al. New J. of Phys. **4** (2002) 28.1.
[60]. T.W. Petrie et al., Nuclear Fusion, **43** (2003), 910.
[61]. R.A.Pitts et al., J. Nucl. Mat., **337-339** (2005) 146.
[62]. R.A.Pitts et al., Nuclear Fusion, submitted (2005a).
[63]. J.I. Paley et al., J. Nucl. Mat., **337-339** (2005) 702.
[64]. V. Riccardo et al., Plasma Phys. Control. Fusion **44** (2002) 905.
[65]. V. Riccardo et al., Plasma Phys. Control. Fusion **45** (2003) A269.
[66]. L. Rosenhead, ed., Laminar Boundary Layers, Oxford U. Press, Oxford, UK (1963).
[67]. D. Rudakov et al., Plasma Phys. Control. Fusion **44** (2002) 717.
[68]. F.C.Schuller, Plasma Phys. Control. Fusion **37** (1995) A135.
[69]. B.Scott, Low frequency fluid drift turbulence in magnetised plasmas, IPP report, **5/92**, Max-Planck Gesselschaft, Garching, Germany (2001).
[70]. P.B. Snyder, H.R.Wilson, Plasma Phys. Control. Fusion **45** (2003) 1671.
[71]. C.Silva et al., J. Nucl. Mat., **337-339** (2005) 722.
[72]. E.R.Solano et al, Plasma Phys. Control. Fusion **46** (2004) L7.
[73]. E.R.Solano et al, J. Nucl. Mat., **337-339** (2005) 747.
[74]. L.Spitzer, R.Harm, Phys. Rev. **89** (1953) 977.
[75]. P.C Stangeby, The Plasma Boundary of Magnetic Fusion Devices, IoP, Bristol (2000).
[76]. T.Tajima, Computational Plasma Physics, Addison-Wesley, New York (1989).
[77]. B.Taylor, Plasma Phys. Control. Fusion **39** (1997) A1.
[78]. H.Thomsen et al., Phys. Plasmas **9** (2002) 1233.
[79]. D.Tskhakaya and S. Kuhn, Contrib. Plasma Phys., **42** (2002) 302.
[80]. D.Tskhakaya et al., Theory of Fusion Plasmas, Ed. J.W. Connor et al, Soc. Italiana di Fisica, Bologna, Italy (2004) 97.
[81]. J.Wesson, Tokamaks, 3rd. Ed., Oxford U. Press, Oxford, UK (2004).
[82]. H. R. Wilson and S. C. Cowley, Phys. Rev. Lett. **92** (2004) 175006.
[83]. X.Q.Xu et al , J. Nucl. Mat., **266-269**, (1999) 993.

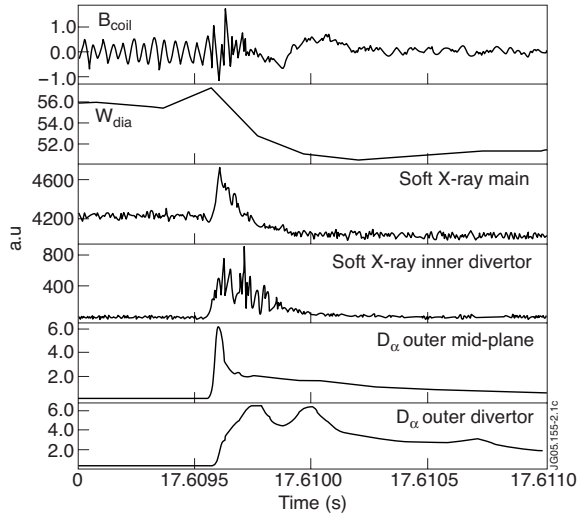

Fig.2.1: Typical Type-I ELM on JET. Signals in descending order: magnetic pick up coil at top of the vessel, plasma stored energy, main chamber soft X-ray, inner divertor soft X-ray, vertical D_α chord passing through the outer mid-plane and looking at outer baffle and outer divertor D_α. The temporal extent of the plot is 2ms.

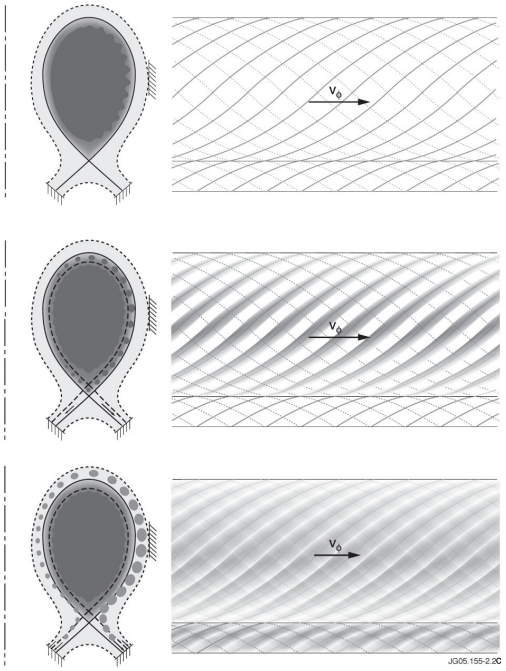

Fig.2.2: Schematic representation of the three stages of ELM evolution: the MHD stage (top), transport stage (middle) and exhaust stage (bottom). The plasma cross-section is shown on the left and a toroidal view is shown on the right. Note that MHD activity and filament formation are largest on the outboard side of the torus. Possible reconnection at the X-point is indicated by the formation of a new separatrix, while parallel losses to the targets are indicated with arrows.

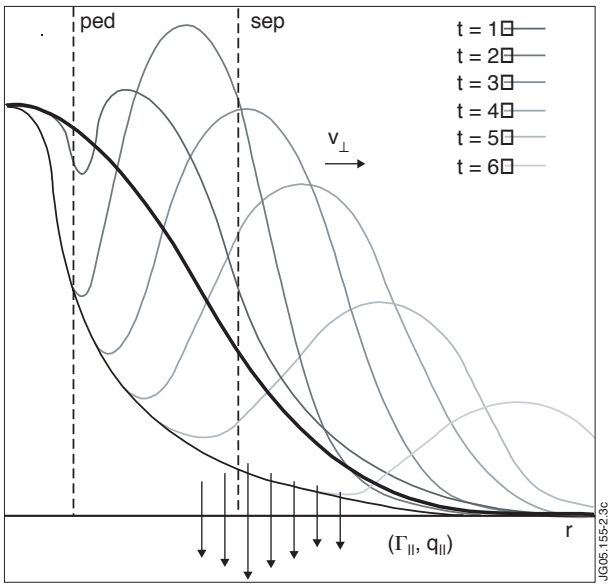

Fig.2.3: Schematic representation of the outer-mid plane density profile evolution: initial (pre-ELM) profile (black), filament formation (dark grey), filament propagation (light grey). Parallel losses are pronounced in the SOL and may be active in pre-ELM pedestal region if reconnection at the X-point has taken place.

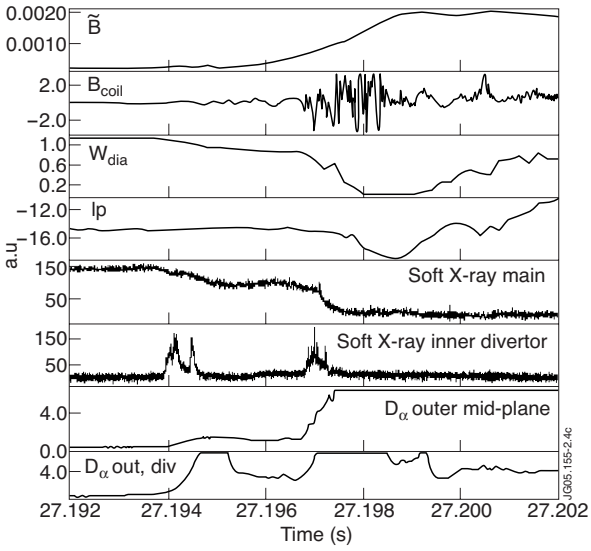

Fig.2.4: Typical disruption on JET (thermal quench at t ~ 67.1972s). Signals in descending order: average magnetic perturbation, magnetic pick up coil at top of the vessel, plasma stored energy, plasma current, main chamber soft X-ray, inner divertor soft X-ray, vertical D_α chord passing through the outer mid-plane and looking at outer baffle and outer divertor D_α. The temporal extent of the plot is 10ms.

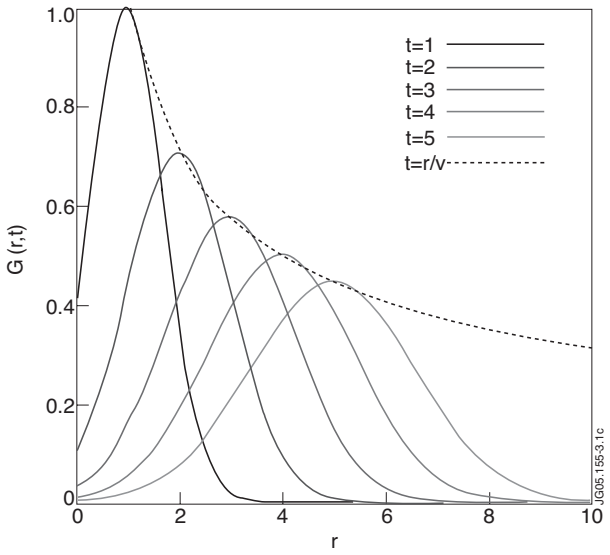

Fig.3.1: Temporal evolution of the Green's function of the SOL, namely an advected Gaussian wave-packet, with $u_\perp = D_\perp = 1$ and negligible parallel losses.

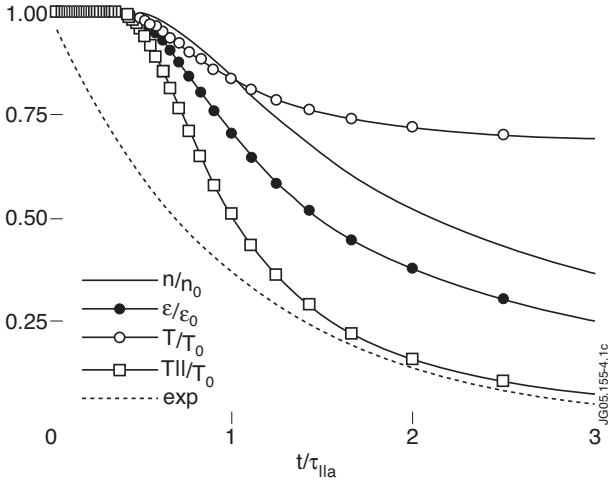

Fig.4.1: Temporal decay of normalised filament density, energy and temperatures for a delta function impulse as a function of time normalised by the parallel transit time, $\tau_{||}a$.

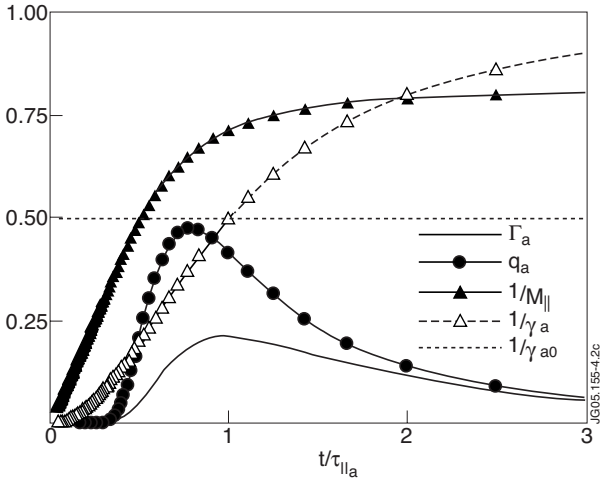

Fig.4.2: Temporal evolution of deposited particle and energy fluxes, the inverse Mach number, and sheath transmission coefficient for a delta function impulse (the steady state value of the latter is indicated by a dotted line).

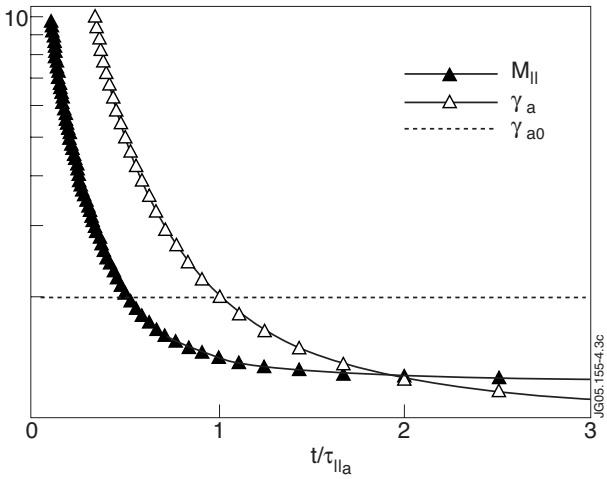

Fig.4.3: Temporal decay of the Mach number and sheath transmission coefficient for a delta function impulse (the steady state value of the latter is indicated by a dotted line).

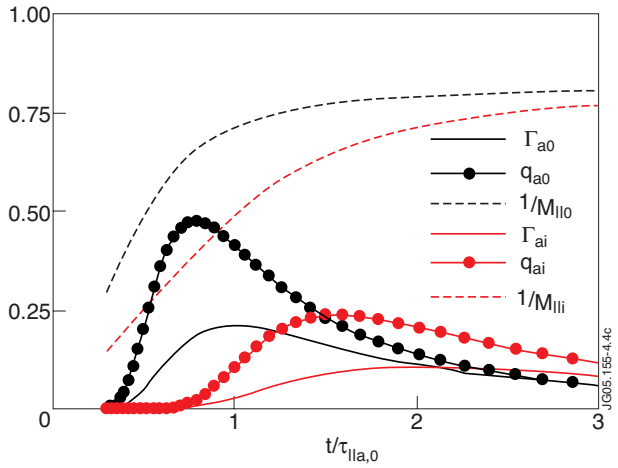

Fig.4.4: Temporal evolution of particle and energy fluxes deposited on the outer and inner divertors; corresponding Mach numbers are also indicated.

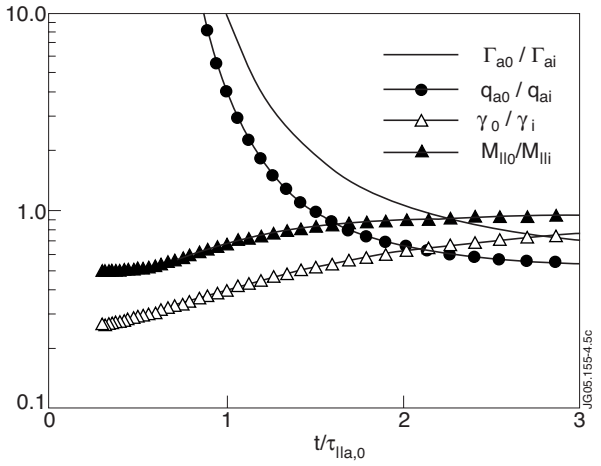

Fig.4.5: Temporal evolution of ratio of outer to inner target deposited particle and energy fluxes, Mach numbers and sheath transmission coefficients for a delta function impulse.

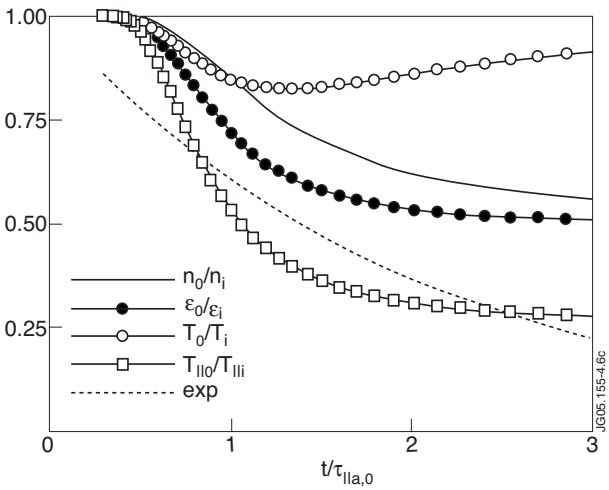

Fig.4.6: Temporal evolution of the ratio of outer to inner filament-half quantities: density, energy and temperatures, for a delta function impulse (pure exponential decay is indicated by a dotted line).

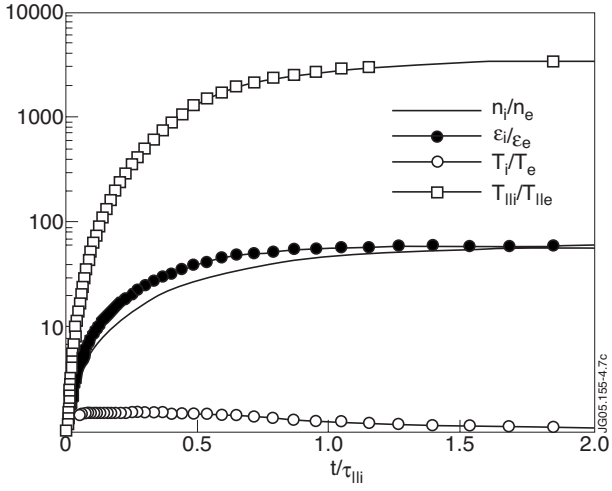

Fig.4.7: Temporal evolution of the ratio of ion to electron quantities: density, energy and temperatures, for a delta function impulse. Time is normalised by the ion parallel loss time.

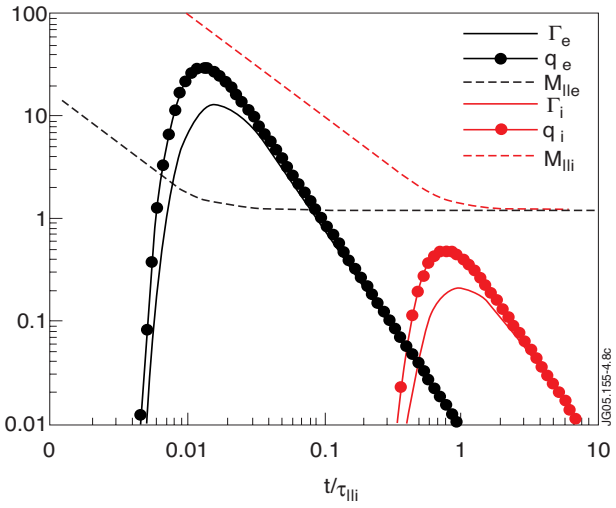

Fig.4.8: Temporal evolution of ion and electron particle and energy fluxes deposited on the outer divertor, for a delta function impulse; corresponding Mach numbers are also indicated.

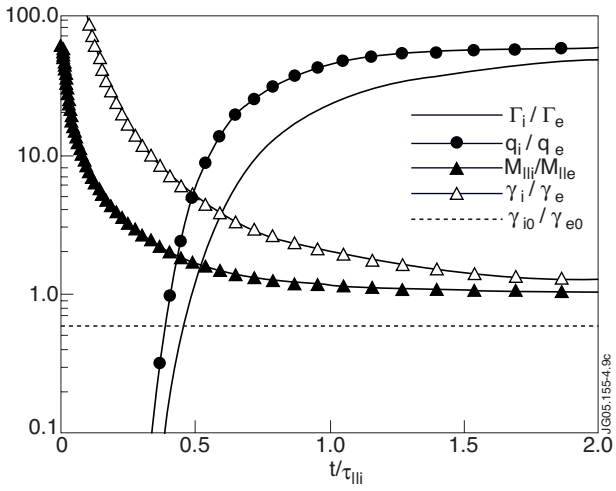

Fig.4.9: Temporal evolution of ratio of ion to electron deposited particle and energy fluxes, Mach numbers and sheath transmission coefficients, for a delta function impulse.

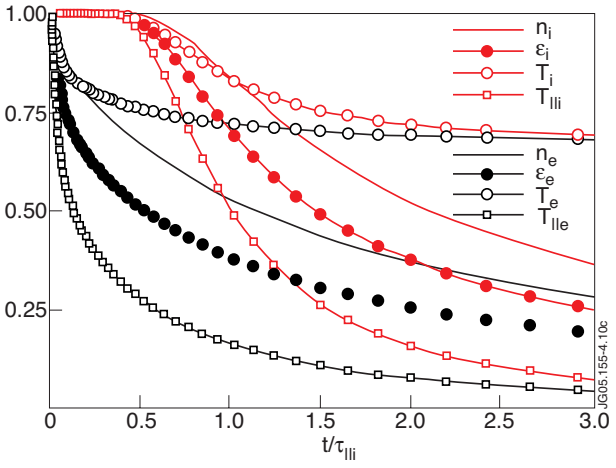

Fig.4.10: Temporal decay of normalised ion and electron filament quantities: density, energy and temperatures for a delta function impulse as a function of time normalised by the parallel ion parallel loss time, $\tau_{||}i$. The results assume the weak quasi-neutrality constraint with y = 1.

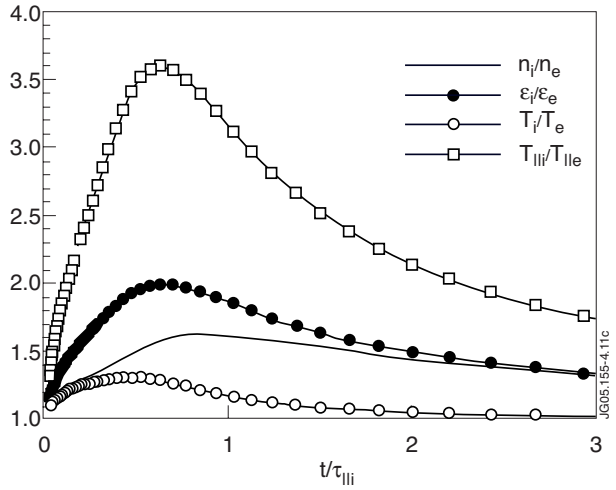

Fig.4.11: Temporal evolution of the ratio of ion to electron quantities: density, energy and temperatures for a delta function impulse, assuming the weak quasi-neutrality constraint with y = 1.

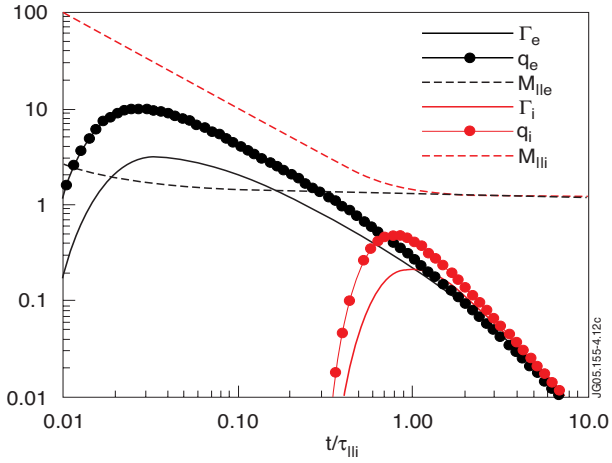

Fig.4.12: Temporal evolution of ion and electron particle and energy fluxes deposited on the outer divertor for a delta function impulse, assuming the weak quasi-neutrality constraint with y = 1.

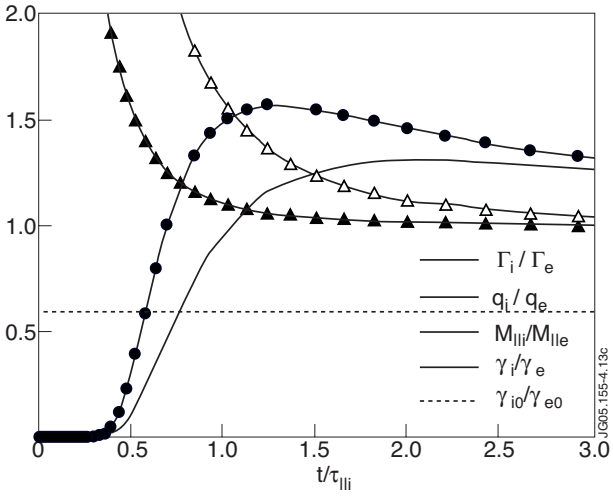

Fig.4.13: Temporal evolution of the ratio of ion to electron deposited particle and energy fluxes, Mach numbers and sheath transmission coefficients for a delta function impulse, assuming the weak quasi-neutrality constraint with y = 1.

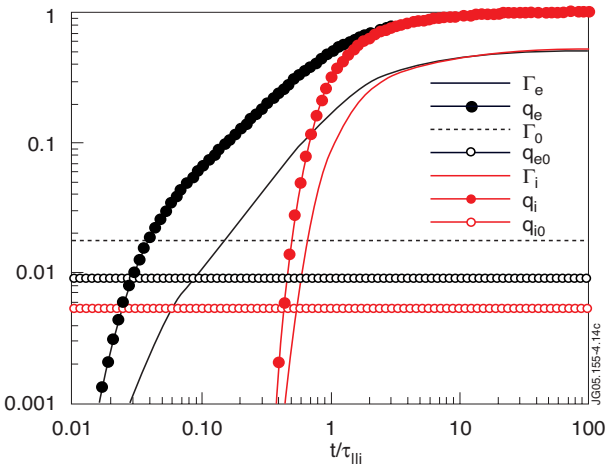

Fig.4.14: Temporal evolution of ion and electron particle and energy fluxes deposited on the outer divertor for a Heaviside impulse, assuming the weak quasi-neutrality constraint with y = 1.

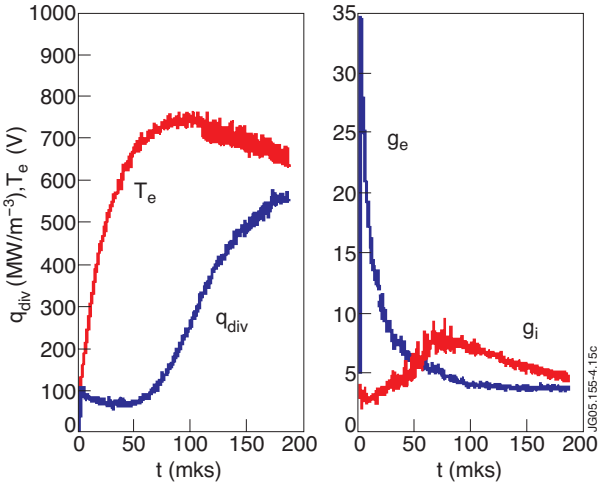

Fig.4.15: Results of PiC simulations of JET Type-I ELM using the BIT1 code showing the temporal evolution of the electron temperature, deposited energy flux and the sheath transmission coefficients [Tskhakhaya04].

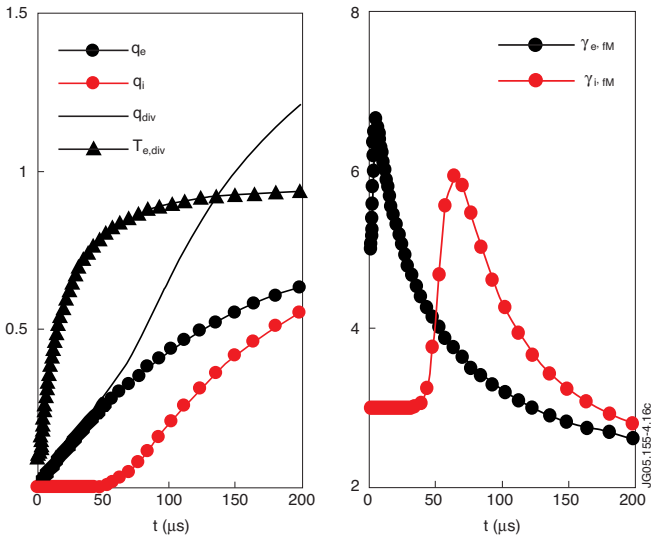

Fig.4.16: Results of the Maxwellian model with simulation of a JET Type-I ELM for same initial conditions as those shown in Fig.4.15, assuming a weak quasi-neutrality constraint with y = 1.7. In addition to the total deposited energy flux, both the electron and ion contributions are shown.

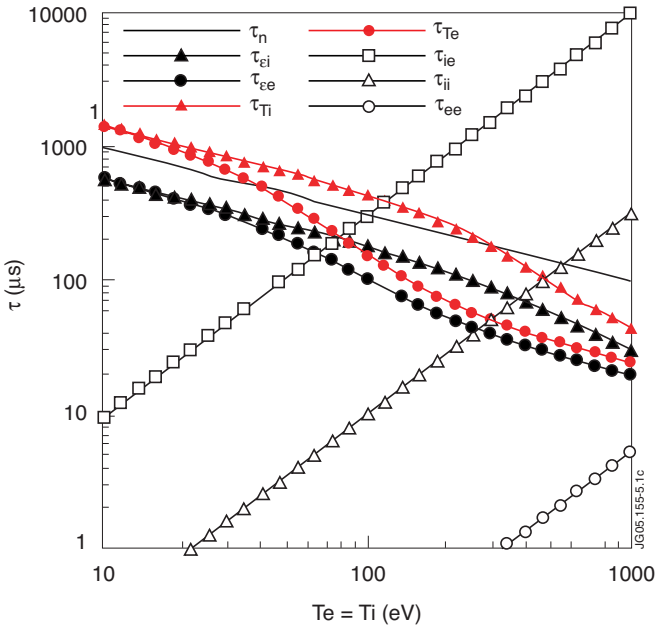

Fig.5.1: Characteristic parallel loss and collisional relaxation times for $n_0 = 10^{20}\ m^{-3}$, $T_{e,0} = T_{i,0} = 1keV$ and $L_{||} \sim \pi R q_{95} \sim 30m$ in the ELM relevant temperature range of 10-1000eV, assuming M = 1, and α_i and α_e chosen such that $\gamma_e \rightarrow \gamma_e^{\infty} \sim 5$ and $\gamma_i \rightarrow \gamma_i^{\infty} \sim 3.5$ as $\nu_e^* \rightarrow 0$.

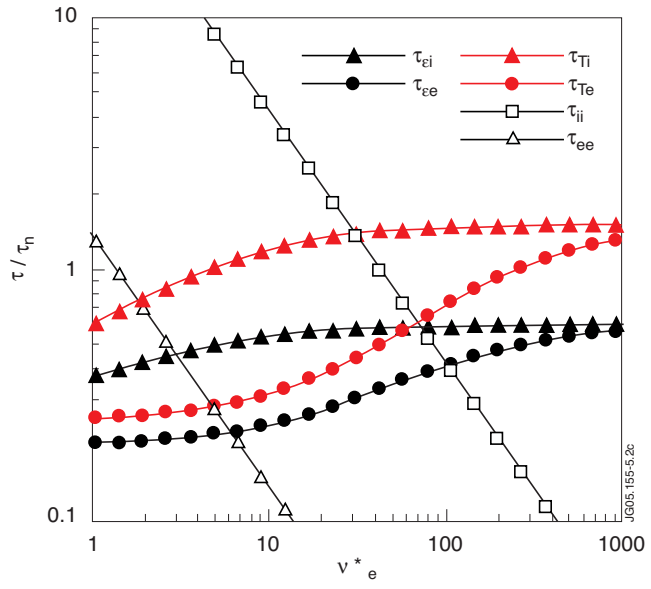

Fig.5.2: The same information as that shown in Fig.5.1, with characteristic times normalised by the density loss time and plotted vs. the electron collisionality.

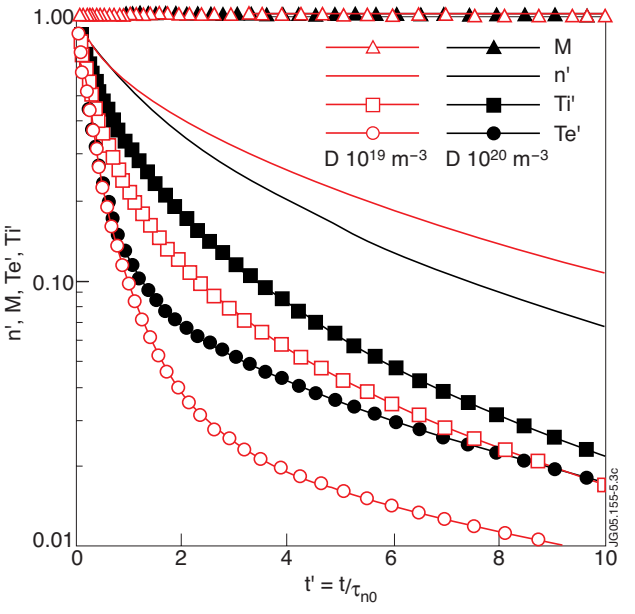

Fig.5.3: Temporal decay of normalised filament quantities (density, Mach number and ion and electron temperatures) based on the results of the fluid model with assumptions of Section 5.2: parallel dynamics with Bohm criterion. Assuming D^+ ions, initial temperatures $T_{e,0} = T_{i,0} = 1keV$ and two values of the initial density: $n_0 = 10^{19}\ m^{-3}$ (open symbols) and $10^{20}\ m^{-3}$ (solid symbols).

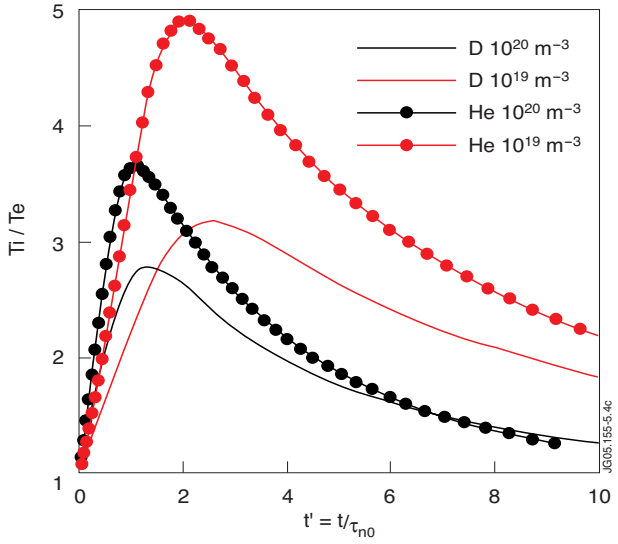

Fig.5.4: Temporal evolution of the ratio of ion and electron temperatures based on the results of the fluid model with assumptions of Section 5.2: parallel dynamics with Bohm criterion. Initial temperatures $T_{e,0} = T_{i,0} =$ 1keV, both D^+ and He^{++} ions and two values of the initial density: $n_0 = 10^{19}\ m^{-3}$ and $10^{20}\ m^{-3}$.

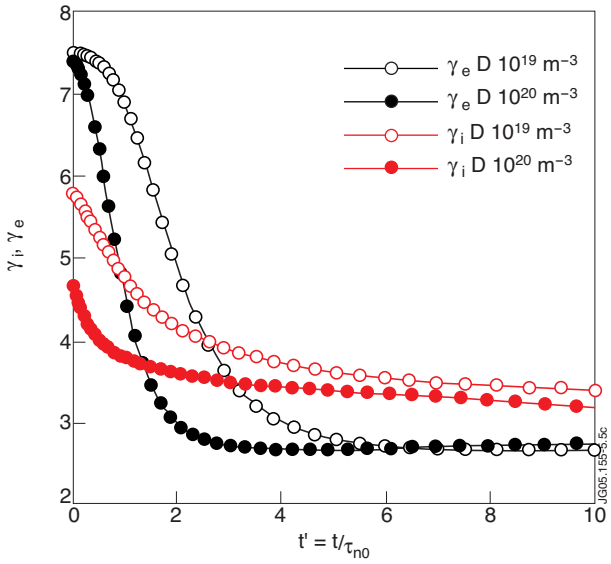

Fig.5.5: Temporal evolution of the sheath transmission coefficients based on the results of the fluid model with assumptions of Section 5.2: parallel dynamics with Bohm criterion. D^+ ions only. Initial temperatures $T_{e,0} = T_{i,0} =$ 1keV, and two values of the initial density: $n_0 = 10^{19}\ m^{-3}$ and $10^{20}\ m^{-3}$.

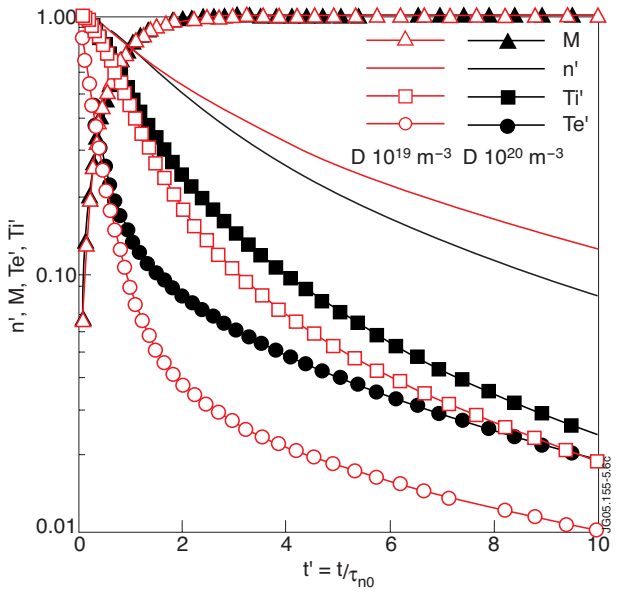

Fig.5.6: Temporal decay of normalised filament quantities (density, Mach number and ion and electron temperatures) based on the results of the fluid model with assumptions of Section 5.3: parallel dynamics with ion delay. Assuming D+ ions, initial temperatures $T_{e,0} = T_{i,0} = 1$ keV and two values of the initial density: $n_0 = 10^{19}\ m^{-3}$ (open symbols) and $10^{20}\ m^{-3}$ (solid symbols).

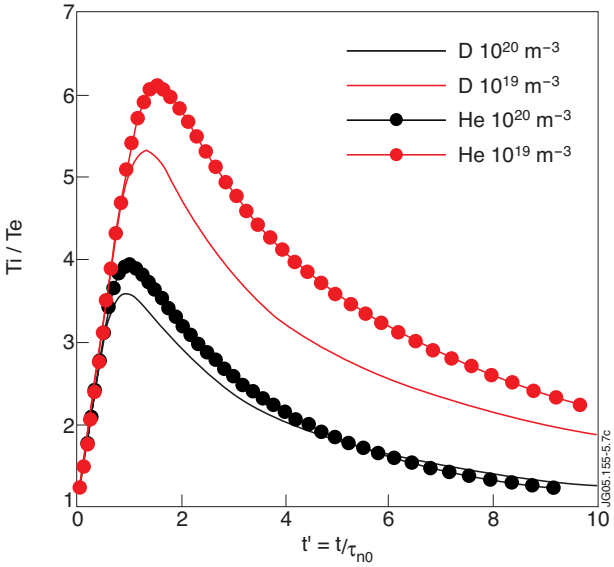

Fig.5.7: Temporal evolution of the ratio of ion and electron temperatures based on the results of the fluid model with assumptions of Section 5.3: parallel dynamics with ion delay. Initial temperatures $T_{e,0} = T_{i,0} = 1$ keV, both D^+ and He^{++} ions and two values of the initial density: $n_0 = 10^{19}\ m^{-3}$ and $10^{20}\ m^{-3}$.

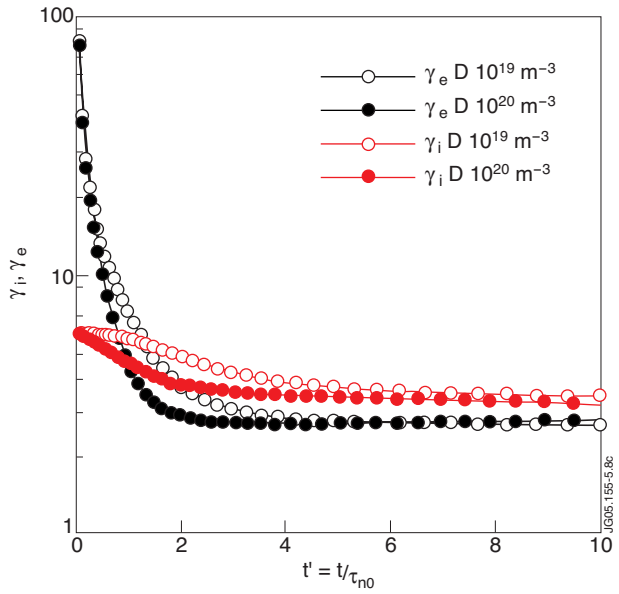

Fig.5.8: Temporal evolution of the sheath transmission coefficients based on the results of the fluid model with assumptions of Section 5.3: parallel dynamics with ion delay. D+ ions only. Initial temperatures $T_{e,0} = T_{i,0} = 1$ keV, and two values of the initial density: $n_0 = 10^{19}$ m^{-3} and 10^{20} m^{-3}.

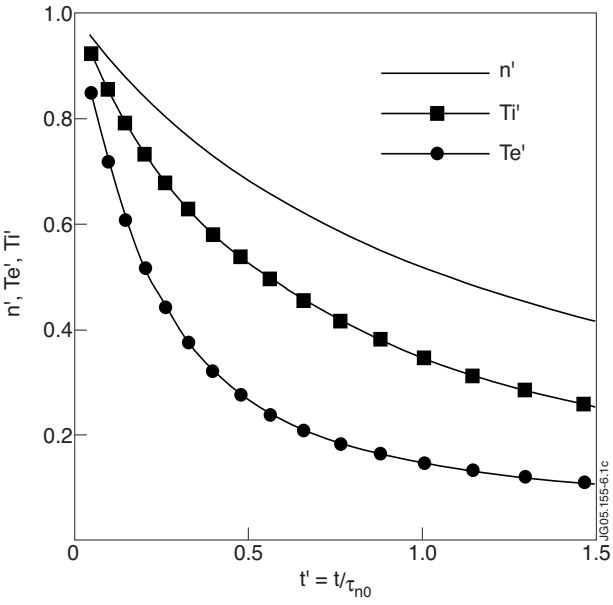

Fig.6.1: JET Type-I ELM modelling for the RFA experiment. Temporal decay of normalised filament quantities (density, ion and electron temperatures) based on the results of the fluid model with assumptions of Section 5.2: parallel dynamics with Bohm criterion. Assuming H+ ions, initial conditions: $T_{e,0} = T_{i,0} = 300$eV, $n_0 = 1.5{\times}110^{19}$ m^{-3}.

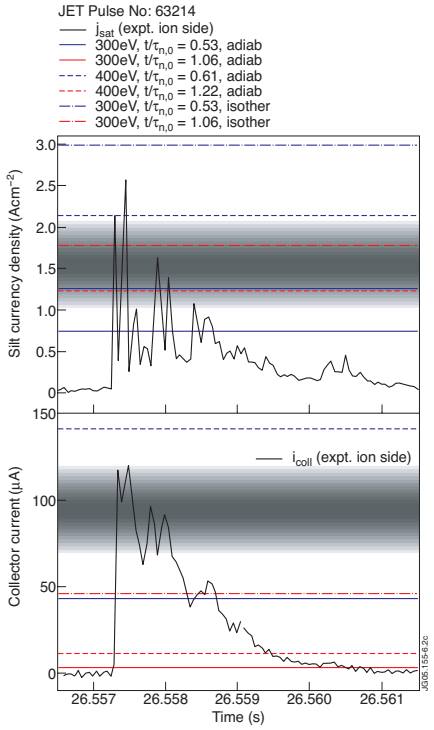

Fig.6.2: JET Type-I ELM experiment vs. modelling comparison. RFA slit ion saturation current density and RFA collector current for a typical Type-I ELM in the discharges considered. The horizontal lines represent predictions of Fig.6.1 with t' ~ 0.45 – 1.1 with filament expansion such that nmax/nint ~0.5 and $T_{max}/T_{int} \sim 0.5^{\gamma-1}$ at $t = t_{RFA}$. Three cases are shown: a) mid-pedestal values (300eV, $1.5{\times}10^{19}$ m^{-3}) with $\gamma = 5/3$, b) the same with $\gamma = 1$, c) pedestal values (400eV, $2.5{\times}10^{19}$ m^{-3}) with $\gamma = 5/3$.

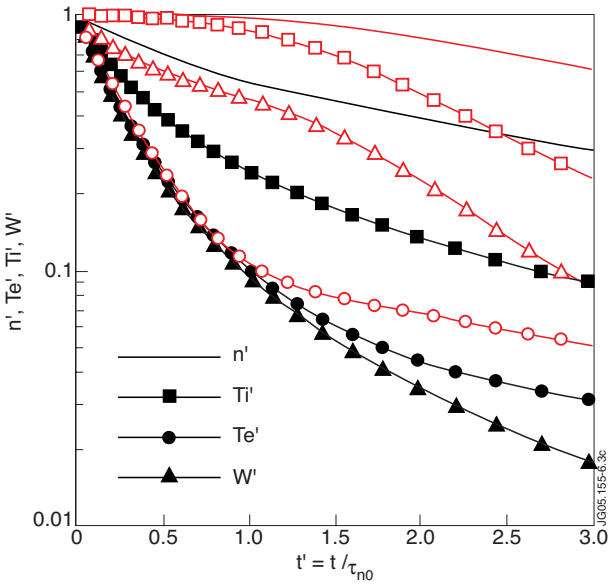

Fig.6.3: ITER type-I ELM prediction. Temporal decay of normalised filament quantities (density, ion and electron temperatures and total energy) based on the results of the fluid model with assumptions of Section 5.2 (solid symbols) and Section 5.3 (open symbols). Assuming D^+ ions, and mid-pedestal initial values: $T_{e,0} = T_{i,0} = 2$keV and $n_0 = 4.5{\times}10^{19}$ m^{-3}.

	JET	ITER	ITER/ JET
A	2	2.5	1.25
Z	1	1	1
R_0 (m)	3.0	6.2	2.1
B_0 (T)	2.4	5.3	2.2
I_p (MA)	2.5	15	6
q_{95}	2.7	3.0	1.1
P_{SOL} (MW)	9.0	75	8.3
n_e (10^{19} m^{-3})	6.5	10	1.54
$n_{e,ped}$ (10^{19} m^{-3})	3.8	6	1.58
$n_{e,sep}$ (10^{19} m^{-3})	1.9	3	1.58
$T_{i,ped}$, $T_{e,ped}$ (keV)	1.5	4	2.66
$T_{e,sep}$ (eV)	100	200	2
$T_{i,sep}$ (eV)	200	400	2
$\nu^*_{e,ped}$, $\nu^*_{i,ped}$	0.036	0.018	0.5
$\nu^*_{e,sep}$	4	3.6	0.9
$\nu^*_{i,sep}$	1	0.9	0.9
β_{ped} (R_{omp})	0.014	0.012	0.85
$\rho_{i,ped}$ (R_{omp}) (mm)	3.1	2.6	0.83
$\rho_{\theta i,ped}$ (R_{omp}) (mm)	10.3	8.6	0.83
$\tau_{A,ped}$ (R_{omp}) (μs)	5.6	8.2	1.46
$\tau_{\|\|,ped}$ (μs)	67	106	1.57
$[\tau_{\|\|}]$ (μs)	186	317	1.7
$\tau_{ii,ped}$ (ms)	1.54	4.73	3.07
$\tau_{E,nc}$ (ms)	20	55–300	2.75–15
$[\tau_E]$ (s)	0.4	3.8	9.5

***Table 2.1**: Nominal pedestal and separatrix parameters for JET and ITER, and the ratio of ITER to JET values. The neo-classical time is evaluated with the two different pedestal width scalings of Table 2.2.*

	JET	ITER	ITER/ JET
$\breve{}_{ped} = 0.025R\ (mm)$	25	50	2
$\rho^*_{i,ped} = \rho_{i,ped} / \breve{}_{ped}$	0.125	0.05	0.4
$\tau_{MHD}^{min}/\tau_{A,ped}$	17	36	2.1
$\tau_{MHD}^{min}\ (R_{omp})\ (\mu s)$	95	297	3.1
$\breve{}_{ped} = 2.5\rho_{\theta i,ped}(R_{omp})(mm)$	25	21	0.83
$\rho^*_{i,ped} = \rho_{i,ped} / \breve{}_{ped}$	0.125	0.125	1
$\tau_{MHD}^{min}/\tau_{A,ped}$	17	20.5	1.2
$\tau_{MHD}^{min}\ (R_{omp})\ (\mu s)$	95	169	1.8

Table"2.2*: Estimated lower limits on the ELM MHD time for JET and ITER with two different pedestal width scalings: Dped /R = 0.025 and Dped /rqi,ped = 2.5, and the ratio of ITER to JET quantities. The estimate is based on equations (2.1) and (2.5). The upper limits, predicted by (2.1) and (2.4) yield tMHDmax ~ 240 ms for JET and ~ 690 ms for ITER.*

	n'	T_i'	T_e'	$W' = n'(T_i' + T_e')$
Bohm	0.58 – 0.45	0.26 – 0.16	0.12 – 0.06	0.11 – 0.05
Modified Bohm	k_i (0.58 – 0.45)	k_i (0.26 – 0.16)	0.12 – 0.06	k_i (0.11 – 0.05)
Bohm delayed by $\tau_{n,0}$	0.97 – 0.9	0.9 – 0.7	0.13 – 0.7	0.5 – 0.35
Maxwellian	0.9 – 0.7	0.55 – 0.45	0.65 – 0.25	0.15 – 0.1

Table 6.1*: Summary of predicted average ELM filament quantities (normalised to initial, mid-pedestal values) at the ITER limiter radius. Here 1 < Ki < 2 is a kinetic correction, weighted towards unity. Normalised peak filament values, assuming polytropic radial expansion with g ~ 4/3, are obtained as nmax'/n' ~ 1/2, Ti.max'/Ti' ~ Te.max'/Te' ~ 0.5g-1.*

	AUG	*JET*	*ITER*
n_{max}'	*0.30*	*0.275*	*0.26*
$T_{i,max}'$	*0.195*	*0.23*	*0.175*
$T_{e,max}'$	*0.07*	*0.09*	*0.07*
n_{max} (m^{-3})	6.9×10^{18}	8.25×10^{18}	1.2×10^{19}
$T_{i,max}$ (eV)	*88*	*185*	*350*
$T_{e,max}$ (eV)	*31*	*74*	*140*
$\tau_{n,max}/\tau_{n0}$	*0.91*	*0.72*	*0.83*
$\tau_{Ti,max}/\tau_{n0}$	*0.82*	*0.635*	*0.64*
$\tau_{Te,max}/\tau_{n0}$	*0.5*	*0.39*	*0.42*
$\lambda_{n,max}$ (mm)	*33.5*	*47*	*54.5*
$\lambda_{Ti,max}$ (mm)	*30*	*41*	*42.5*
$\lambda_{Te,max}$ (mm)	*18.5*	*25*	*27.5*

Table 6.2: *Summary of predicted peak ELM filament quantities at the nominal limiter radii for three large tokamaks, with the initial conditions and average filament radial velocities as given in section 6.2. The filament was assumed to expand polytropically with g ~ 4/3 and nmax' /n' ~ 0.5 at the limiter radius.*